UNIVERSITY OF CALIFORNIA
RIVERSIDE

Electromechanical Resonators in Graphene Nanoribbons

A Dissertation submitted in partial satisfaction
of the requirements for the degree of

Doctor of Philosophy

in

Physics

by

Yi Wu

March 2017

Dissertation Committee:

Dr. Marc Bockrath , Co-Chairperson
Dr. Shan-Wen Tsai, Co-Chairperson
Dr. Ward Beyermann

The Dissertation of Yi Wu is approved:

Co-Chairperson

Co-Chairperson

University of California, Riverside

Acknowledgments

I would like to thank my advisor, Professor Marc Bockrath. Without his guidance, I would not have been here and finished the amazing five-year journey. A Ph.D. career is never easy, but his deep understanding of physics, patience explanation and skills of doing experiments always guide me through the difficulties and progress. He trusts his students completely even if they have different ideas, and support them with all resources he has. Marc provided me with research direction, technical support, and most importantly, an example of being a professional and nice man. I feel grateful and fortunate to spend the last five years under his supervision.

I would also like to thank the committee members who joined my defense and candidacy exams: Professor Ward Beyermann, Professor Jianlin Liu, Professor Shan-Wen Tsai and Professor Stephen Wimpenny. In addition, I would like to give special thanks to Professor Chun Ning Lau for allowing me to use her equipments.

My research could never progress without the contribution from my colleagues. I'd like to thank Dr. Bin Cheng, Dr. Peng Wang, Dr. Tengfei Miao, Dr. Juan Aguilera, Dr. Oleg Martynov, Dr. Yong Wu, Dr. Cheng Pan, Adrian Nosek, Sean Nelson, Rui Lyv and Nan Zhang for invaluable discussions and technical supports. My thanks also go to all Professor Lau's group members for their assistance and advises.

I would like to also thank UC, Riverside cleanroom staffs, especially Dr. Dong Yan, for maintaining and providing a wonderful working place.

My graduate life would not been complete without the love and support from my family. Thank you Na for being a caring wife who always gets my back. Thank you

Wenyuan for being my little sunshine and bringing me happiness. I can never forget the thrill feeling when I first time see your face. You are the ultimate purpose of working because I hope you will say someday proudly, "I would like to be the man like my dad!"

To my family for all the support.

ABSTRACT OF THE DISSERTATION

Electromechanical Resonators in Graphene Nanoribbons

by

Yi Wu

Doctor of Philosophy, Graduate Program in Physics
University of California, Riverside, March 2017
Dr. Marc Bockrath , Co-Chairperson
Dr. Shan-Wen Tsai, Co-Chairperson

Graphene is a carbon based material that has only one atomic layer. It has exceptional electronic and mechanical properties which makes itself an ideal system to study nanoelectromechanical behaviors. In this work I present the fabrication techniques to create a suspended graphene device. Other than the traditional e-beam lithography, I also present shadow mask technique, a fabrication method enables lithography-free and rapid fabrication. I fabricated single layer graphene resonators in nanoribbon geometry and studied the nonlinear damping oscillation at different temperatures.

Contents

List of Figures **x**

1 Introduction **1**
1.1 Introduction . . . 1
1.2 Graphene Electrical Properties . . . 3
1.3 Graphene Mechanical Properties . . . 5
1.4 Linear Damping and Oscillations . . . 6

2 Device Fabrication **9**
2.1 Introduction . . . 9
2.2 Silicon Wafer . . . 11
2.3 Graphene Exfoliation . . . 12
2.4 Graphene Geometry Definition . . . 12
2.4.1 Landmark . . . 12
2.4.2 Spin Coating . . . 14
2.4.3 Pattern Defining . . . 14
2.4.4 Graphene Etching . . . 15
2.5 Electrode Fabrication . . . 16
2.5.1 Spin Coating . . . 16
2.5.2 Pattern Definition . . . 16
2.5.3 Metal Deposition . . . 18
2.5.4 Lift-off . . . 19
2.6 Suspension . . . 20
2.7 Current Annealing . . . 22

3 Shadow Mask **24**
3.1 Introduction . . . 24
3.2 Mask Fabrication . . . 25
3.2.1 Silicon Wafer . . . 25
3.2.2 Pattern Definition . . . 26
3.2.3 Etching . . . 27
3.3 Mask Usage . . . 28

3.4 Conclusion 32

4 Measurement Techniques and Setup **33**
4.1 Introduction 33
4.2 Electrical Actuation 34
4.3 Electrical Readout 36
4.4 Amplitude Modulation 38
4.5 Frequency Modulation 40
4.6 Experimental Setup 46
4.6.1 Circuit Design 47
4.6.2 Equipment Setup 48

5 Nonlinear Dynamics at Various Temperatures **51**
5.1 Introduction 51
5.2 Nonlinear Dynamics 52
5.2.1 Nonlinearity Due to External Potential 52
5.2.2 Nonlinearity Due to Geometry 53
5.2.3 Nonlinear Behavior 54
5.3 Nonlinear Parameters 57
5.4 Nonlinear Mechanics at Various Temperatures 60

6 Conclusions **63**
6.1 Conclusion 63
6.2 Future Work 64

Bibliography **65**

List of Figures

1.1 Graphene can is the building block for all other dimensions. 2
1.2 Graphene lattice 3
1.3 Graphene band structure. 5

2.1 Different geometries of suspend graphene NEMS 10
2.2 An optical image of graphene on Si/SiO_2 substrate 11
2.3 A schematic diagram of the fabrication process of etching graphene to the desired geometry. 13
2.4 A SEM images of graphene after ICP etching 15
2.5 A schematic diagram of the fabrication process to create electrodes and suspend graphene. 17
2.6 Exposure result of using PMMA/PMMA and MMA/PMMA as e-beam lithography resist. 18
2.7 A schematic diagram of the wafer after metal deposition. 19
2.8 A SEM image of a suspended graphene nanoribbon. 21
2.9 Transport properties before and after current annealing. 23

3.1 A schematic diagram of the fabrication process of shadow masks. 29
3.2 Pictures of finished shadow masks. 30
3.3 A side view of the alignment stage. 31
3.4 Usage of shadow masks and a optical image of finished devices. 32

4.1 A schematic diagram of the graphene nanoribbon resonator system as a parallel plate capacitor. 35
4.2 A schematic diagram of the measurement circuit. 47
4.3 A picture of the internal stick of the home made cryostat. 49

5.1 Duffing coefficient sign change at different source-drain voltage. 55
5.2 Magnitude and phase response to frequency in Duffing oscillators. 56
5.3 FM mixing current magnitude verses frequency at different bias voltage. . . 58
5.4 Transconductance measurement on graphene nanoribbon at low temperature. 59
5.5 Resonance frequency vs. resonance amplitude at different temperatures. . . 61
5.6 Resonance frequency vs. resonance peak width at different temperatures. . 62

Chapter 1

Introduction

1.1 Introduction

Graphene is a novel material made of only one layer of carbon atoms. Different from the bulk form of three-dimensional(3D) materials, this new form is called a two-dimensional(2D) material. Due to its reduced dimensionality, people expect such materials to open new opportunities to probe the material science, build a novel platform for physics research and create dedicated industrial applications.

The theoretical study on graphene can be dated back to 1940s [31][42][46]. But it was long ignored by the mainstream physics community and even predicted that 2D materials cannot exist in the free state because thermal fluctuations should destroy long-range order, resulting in melting of a 2D lattice at any finite temperature [24]. However, graphene was unexpectedly discovered in 2004 [36], and has been the hottest topic in condensed matter physics since then.

Carbon atoms form very strong bonds in the layers and weak bonds between layers.

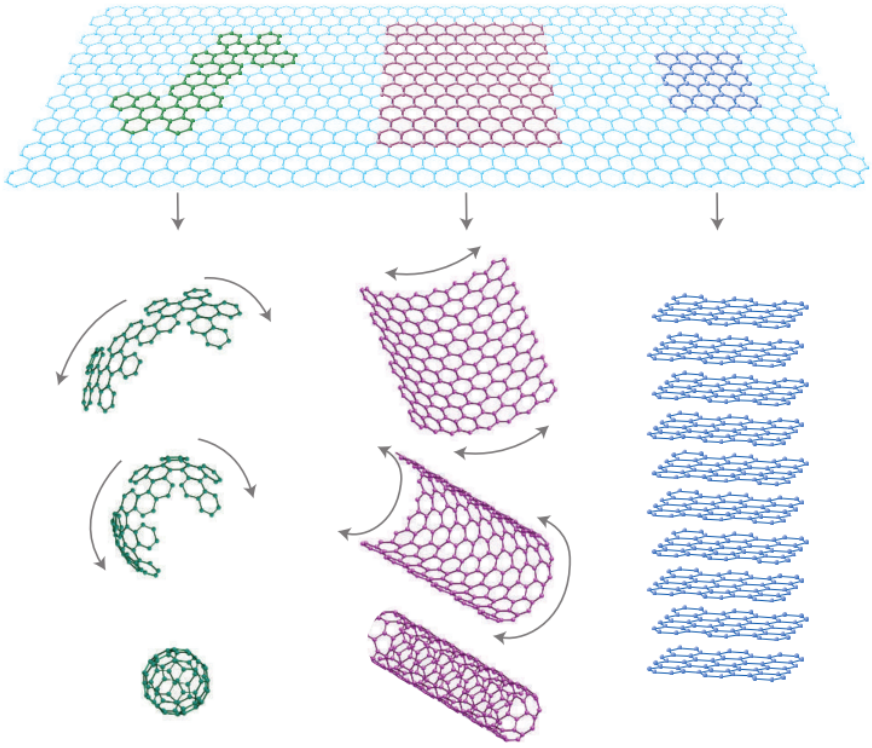

Figure 1.1: Graphene can is the building block for carbon materials of all other dimensions. It can be warped to 0D balls, rolled to 1D nanotubes or stacked to 3D graphite. The graph is adapted from paper [16].

Weak interlayer interactions ensure a single layer of carbon atoms can be isolated from the bulk. And strong intralayer ensure the single layer of atoms can exist in free stand and can even be warped to other dimensions (Figure 1.1).

The graphene 'gold rush' not only reveals the condensed matter physics on a small scale, but also leads to discovery and research on many other 2D materials and heterostructures, too. It's safe to say that the emergence of graphene results in many active and prosperous material studies and applications nowadays.

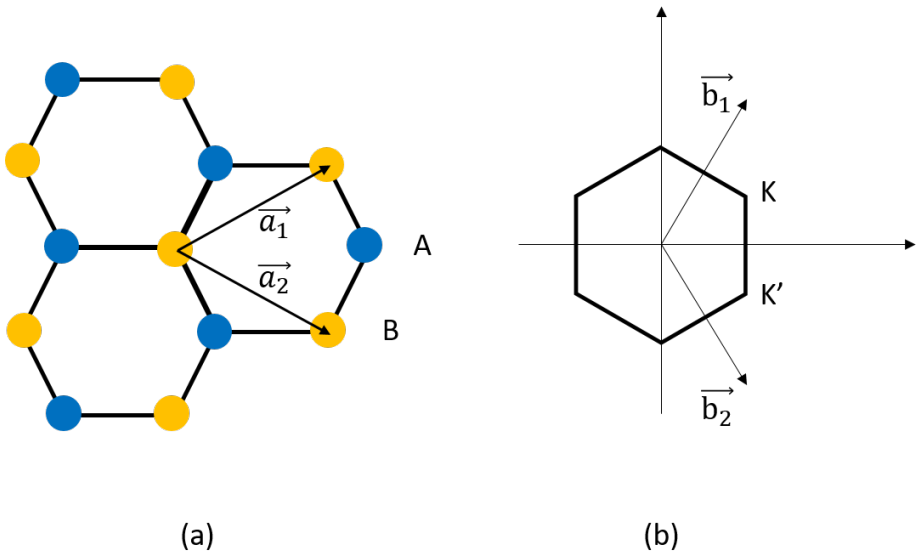

Figure 1.2: Graphene lattice and its Brillouin zone. (a) Graphene lattice structure. A, B are the two non-equivalent atoms, $\vec{a_1}$ and $\vec{a_2}$ are the two lattice vectors. (b) Graphene Brillouin zone. $\vec{b_1}$ and $\vec{b_2}$ are the two reciprocal vectors. K and K' are Dirac points.

1.2 Graphene Electrical Properties

Graphene is made of carbon atoms arranged in repeated hexagonal structures, shown as Figure 1.3. There are two atoms in each unit cell. The lattice vectors can be written as

$$\vec{a}_1 = \frac{a}{2}(3, \sqrt{3}), \quad \vec{a}_2 = \frac{a}{2}(3, -\sqrt{3}) \tag{1.1}$$

where $a \approx 1.42$Åis the carbon-carbon distance. The reciprocal vectors can be easily calculated to be

$$\vec{b}_1 = \frac{2\pi}{3a}(1, \sqrt{3}), \quad \vec{b}_2 = \frac{2\pi}{3a}(1, -\sqrt{3}) \tag{1.2}$$

Corresponding to A and B in real space lattice, K and K' are two distinct posi-

tions in reciprocal lattice. They are call Dirac points because, according to tight-binding calculation results, the valence band and conduction band touch at these two points. The energy spectrum is [46]

$$E_{\pm}(k) = \pm t\sqrt{3 + f(k)} - t'f(k) \tag{1.3}$$

where the plus sign refers to the upper band and the minus sign refers to the lower band, and

$$f(k) = 2cos(\sqrt{3}k_y a) + 4cos(\frac{\sqrt{3}}{2}k_y a)cos(\frac{3}{2}k_x a) \tag{1.4}$$

The dispersion can be obtained by expanding the energy in a vicinity of K or K' and leads to

$$E_{\pm}(q) \approx \pm v_F|q| + O[(q/K)^2] \tag{1.5}$$

where q is the momentum measured relatively to the Dirac points and v_F is the Fermi velocity. The most remarkable result from this equation is that the energy is a linear function of the momentum q. The conduction band and valence band intersect at $q = 0$, which makes graphene a zero-gap semiconductor. The carrier density can be tuned by an external electrical field. When the external field changes, the carrier density changes accordingly, and causes a change in the graphene conductivity.

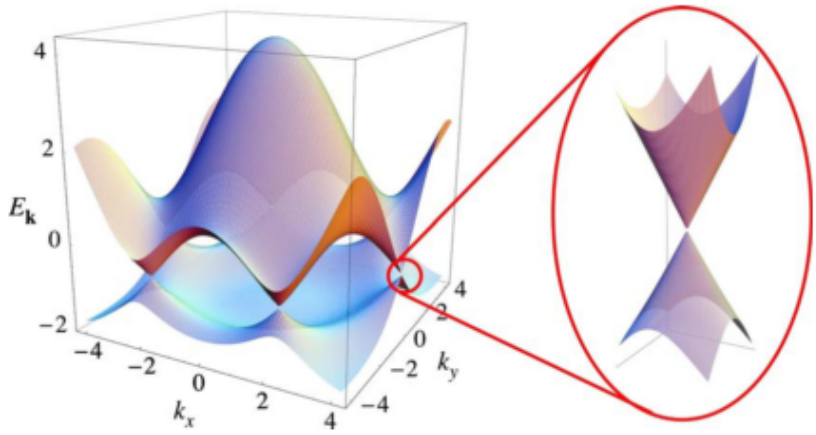

Figure 1.3: Calculated graphene band structure according to tight-binding model. The inset is the zoom in view of one of the Dirac points. The graph is adapted from paper [35].

1.3 Graphene Mechanical Properties

Though it contains only one atom layer, graphene exhibits extremely strong mechanical properties. Measurements confirmed graphene has a tensile strength of 130 GPa, which corresponds to a Young's modulus of 1 TPa [26]. This value is higher than any other known materials. Graphene has a flexural rigidity of 3.18 GPa·nm^3 [45] and breaking strength of 130 GPa, while the mass density is only 7.4×10^{-19} kg/μm^2. With a thickness of regular kitchen towel, graphene sheet would be able to hold an elephant standing on top of a pencil. The high stiffness and low mass of graphene lead to a high resonant frequency. The way people exploit graphene's good mechanical properties is to make nanoelectromechanical systems (NEMS) out of it.

NEMS are the successor of microelectromechanical systems (MEMS). With the device scale down from micrometers to nanometers, the system consumes less power, has higher integrity abilities and is able to perform more precise measurements. NEMS have

been proven useful particularly in ultrasensitive mass sensing [9][25] and exploring quantum phenomena at low temperature [23][38][44].

1.4 Linear Damping and Oscillations

The simple harmonic oscillator is the simplest and coarsest estimation to any oscillation system. We usually use it to approximate small oscillations in frictionless environments. People made use of the stable frequency in those oscillations and invented numerous tools and changed our life profoundly. For example, pendulum clocks have been the world's most precise timekeeper for three centuries [30], and is continuing to be an important furniture in many homes. And in the Foucault pendulum experiment, people proved that earth is spinning for the first time.

The equation of motion of a simple harmonic oscillator is

$$m\ddot{z} + m\omega_0^2 z = F \tag{1.6}$$

where m is the mass of the oscillator, $\ddot{z}$ is the acceleration, $m\omega_0^2 z$ is the restoring force and F is the external force.

If we consider a linear friction, i.e. a friction depends on the velocity, we have an extra term in the equation of motion and it becomes

$$m\ddot{z} + m\omega_0^2 z + \Gamma\dot{z} = F \tag{1.7}$$

where $\Gamma\dot{z}$ is the friction.

In NEMS, the damped oscillator is driven by an external AC force. Assume $F =$

$F_0 \cos(\omega t)$, where ω is the AC frequency. Consider its complex form $F = F_0 e^{i\omega t}$ and let $\gamma = \Gamma/m$, we have

$$\ddot{z} + \omega_0^2 z + \gamma \dot{z} = \frac{F_0}{m} e^{i\omega t} \tag{1.8}$$

The solution to the above equation has two parts, a transient part z_t and a steady-state part z_s. We first set the driving force to be 0 and solve the homogeneous equation to find z_t

$$\ddot{z} + \omega_0^2 z + \gamma \dot{z} = 0 \tag{1.9}$$

Assume $z = Ae^{i\omega t}$ and yield

$$-\omega^2 + \omega_0^2 + i\gamma\omega = 0 \tag{1.10}$$

Solve the above equation and we find

$$\omega = \pm\sqrt{\omega_0^2 - \gamma^2/4} + i\gamma/2 \tag{1.11}$$

This leads to

$$z_t = Ae^{-\frac{\gamma}{2}t} cos(\sqrt{\omega_0^2 - \frac{\gamma^2}{4}}t + \phi_t) \tag{1.12}$$

where A and ϕ_t is determined by initial conditions. Clearly, the oscillation decays with rate $\frac{\gamma}{2}$.

Now we assume $z = Be^{i\omega t}$ and insert it into equation 1.8 to find z_s.

$$B(-\omega^2 + \omega_0^2 + i\omega\gamma) = \frac{F_0}{m} \tag{1.13}$$

This yields

$$B = \frac{F_0/m}{-\omega^2 + \omega_0^2 + i\omega\gamma} \tag{1.14}$$

Express B in exponential notation, $|B|e^{i\phi_s}$, with ϕ_s is the phase of the response relative to the driving force, we have

$$|B| = \frac{F_0/m}{\sqrt{(\omega_0^2 - \omega^2)^2 + \omega^2\gamma^2}} \tag{1.15}$$

$$\tan(\phi_s) = \frac{\gamma\omega}{\omega^2 - \omega_0^2} \tag{1.16}$$

It can be shown that

$$Q = \frac{\omega_0}{\gamma} \tag{1.17}$$

where Q is the quality factor of the oscillator. Therefore, we have the final form of the steady state solution z_s.

$$z_s = \frac{F_0/m}{\sqrt{(\omega_0^2 - \omega^2)^2 + (\omega\omega_0/Q)^2}} \cos(\omega t + \phi_s) \tag{1.18}$$

Harmonic oscillator is the simplest approximation to the practical resonator in nanoelectromechanical systems when the resonator is driven with small amplitude. When the amplitude is driven large, it will enter nonlinear oscillation regime, which will be discussed later in the thesis.

Chapter 2

Device Fabrication

2.1 Introduction

Nanoelectromechanical systems (NEMS), is considered the next generation of microelectromechanical systems (MEMS). Compared to MEMS, NEMS not only cut down the cost, consumes less power, can to be integrated to more sophisticated circuits, but also is more sensitive to small signals. However, smaller scale fabrication techniques has to be introduced to create nano-scale systems.

Among many geometries of NEMS (Figure 2.1), we choose doubly clamped beam to be our research object because its fabrication technique is relatively straightforward. To eliminate edge modes and focus on the fundamental mechanical mode, we further decrease the graphene width and create nanoribbons. In this chapter we will discuss the fabrication techniques and procedure of making a doubly clamped graphene nanoribbon.

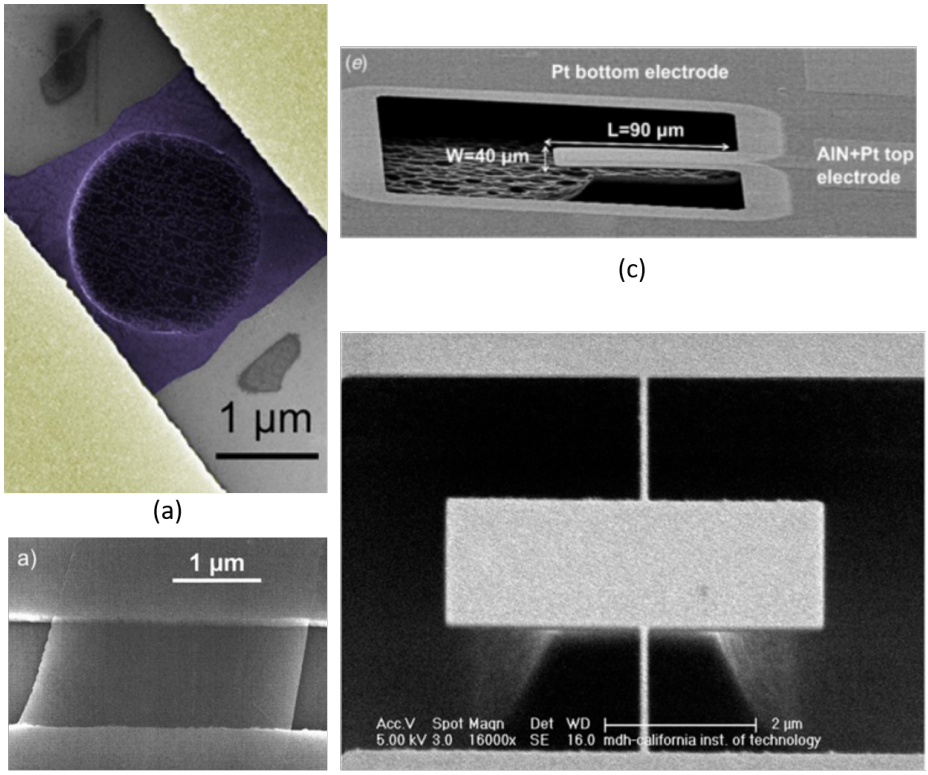

Figure 2.1: Different geometries of suspended NEMS. (a) Drum structure [33]. (b) Doubly clamped beam structure [14]. (c) Cantilever structure [21]. (d) Paddle structure [47].

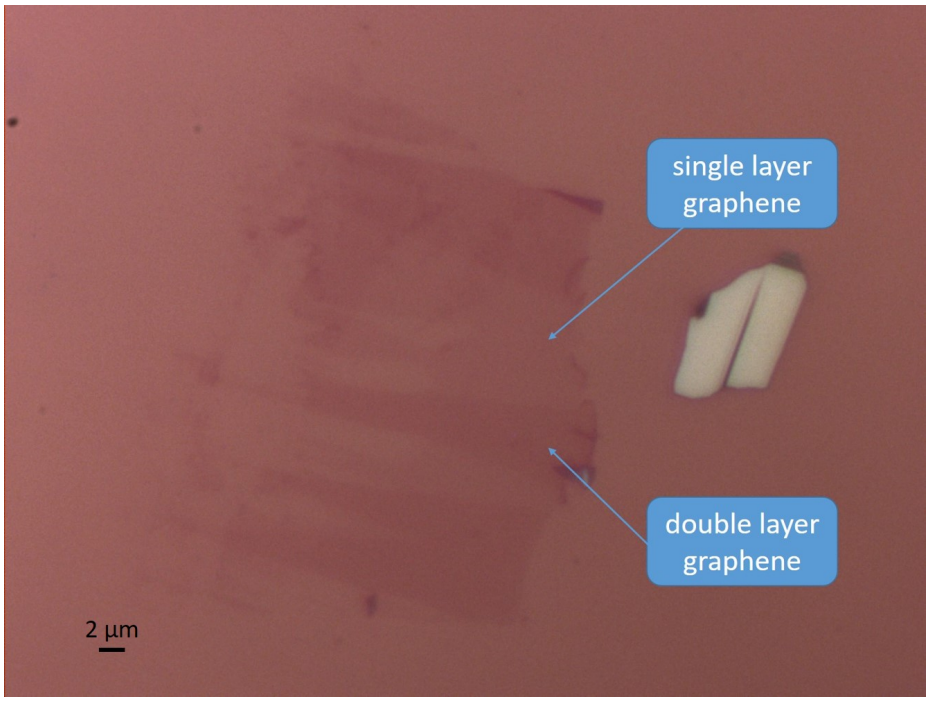

Figure 2.2: An optical image of graphene on Si/SiO_2 substrate. The darkness of purple color indicates the number of layers of graphene.

2.2 Silicon Wafer

Graphene is a one-atom thick material that is nearly transparent. It can not be seen by naked eye in most circumstances, and people have to use sophisticated equipment like SEM or TEM to see them. However, when graphene is supported by a silicon wafer with 300 nm silicon-dioxide (SiO_2) layer, it appears to be light purple in optical microscope. People can even estimate the number of layers based on how dark the purple is.

Silicon wafers are cut from the no-oxide side with diamond pen into small pieces, usually 1 cm $\times$ 1 cm. Then they are cleaned in an ultrasonic bath in acetone followed by isopropyl alcohol (IPA). Finally they are blown dried with nitrogen gas.

2.3 Graphene Exfoliation

People often use transfer or direct exfoliation to put graphene on a wafer. When a large area of graphene is required in the experiment, for example, research on large domain size crystals based on CVD graphene [28], or when graphene has to be put on a specified location, transfer technique serves the purpose best. However, when the required graphene size is small and graphene quality is crucial, people often use direct exfoliation. The easiest and most widely used method is the "scotch tape method".

To perform scotch tape method, Kish graphite is placed on a strip of scotch tape. We fold the tape repeatedly to distribute the graphite evenly on it. We then put a piece of cleaned wafer on the tape, press and scratch them from the back. After that, wafers are removed from the tape carefully and annealed with oxygen at 350 °C for 3 hours to remove the tape residue.

2.4 Graphene Geometry Definition

As shown in Figure 2.2, exfoliated graphene is usually too large or not a geometry we can directly make use of. We can use inductively coupled plasma (ICP) to etch the graphene to be the desired geometry. The process is shown in Figure 2.3.

2.4.1 Landmark

To reference the etching location and the electrode location (later in the chapter), a set of landmarks is often created near the graphene. The fabrication procedure is the same as the procedure for the electrodes, which will be discussed in detail later in the chapter.

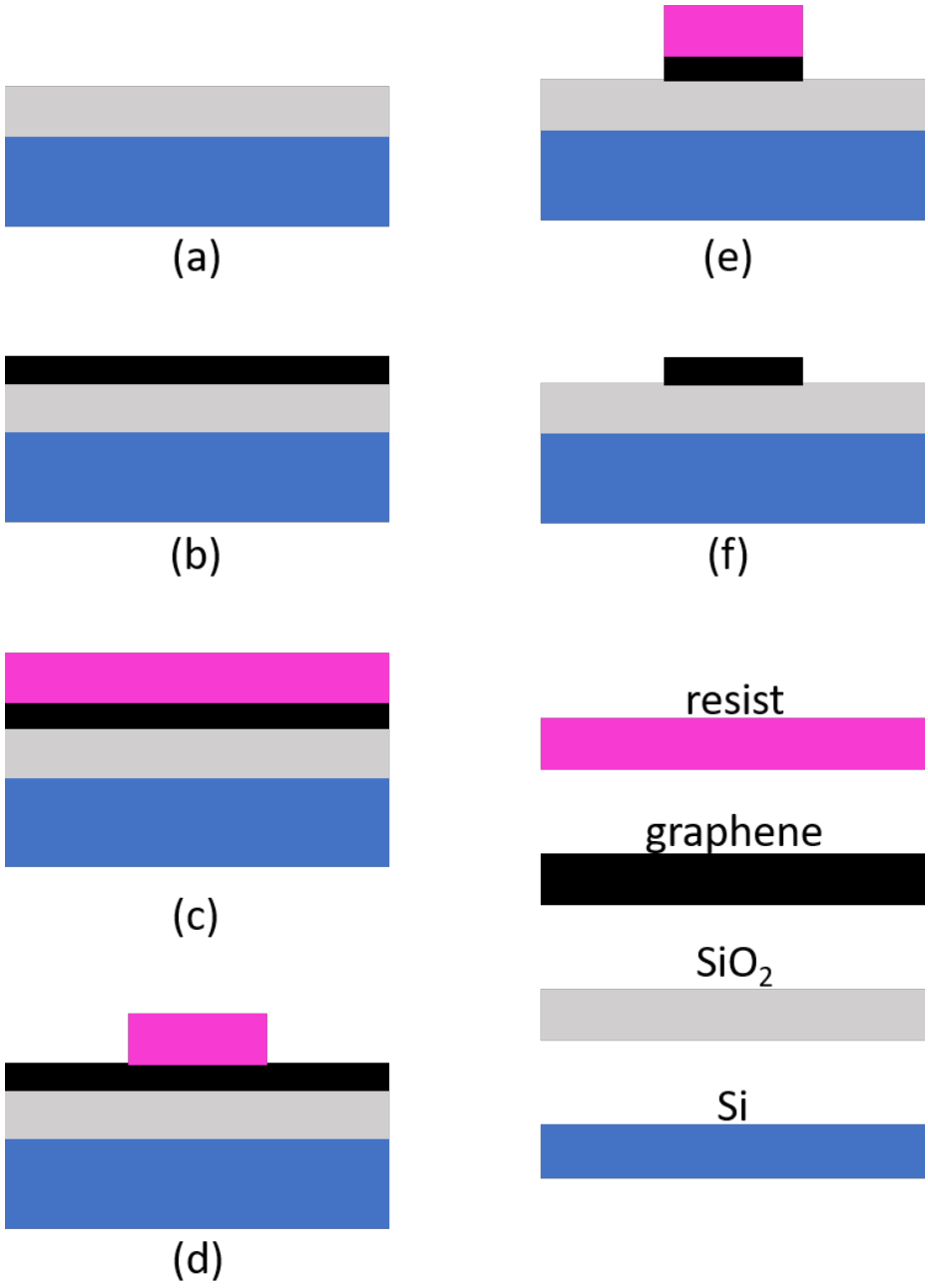

Figure 2.3: A schematic diagram of the fabrication process of etching graphene to the desired geometry. (a) Bare Si/SiO_2 wafer. (b) Exfoliate graphene on the wafer. (c) Spin coat e-beam resist on the wafer. (d) Define the pattern in resist using EBL. Develop the pattern in developer. (e) Etch the exposed graphene with ICP. (f) Remove the resist with hot acetone bath.

2.4.2 Spin Coating

When performing an etching or metal deposition, we use e-beam lithography to open a window in the resist layer, and use the resist as a mask to allow etching plasma or metal atoms to contact only the graphene in the window. We use a bilayer of Poly(methyl methacrylate) (PMMA) as the resist mask. PMMA is a widely used e-beam lithography resist which allows finer structures than other resists. We use PMMA/PMMA layers, as opposed to MMA/PMMA layers, to achieve uniform exposure.

Each layer is spun at 1000 rpm/s ramp-up rate and 4000 rpm rotational speed to ensure a thickness of 180 nm. After each spin coating, the wafer is baked at 180 °C for 10 minutes.

2.4.3 Pattern Defining

We use e-beam lithography to draw patterns on e-beam resist. The procedure is the same as defining electrodes, which will be discussed later in the chapter.

We draw etch patterns to cover the unwanted graphene. If the unwanted graphene area is large, we need to use two or more sets of current and dose based on pattern size and distance to the desired graphene position, so as to balance between lithography speed and pattern resolution.

The wafer is then developed in MIBK/IPA (1:3) solution for 70 seconds and rinsed in IPA solution for 70 seconds to allow the exposed resist to be washed away.

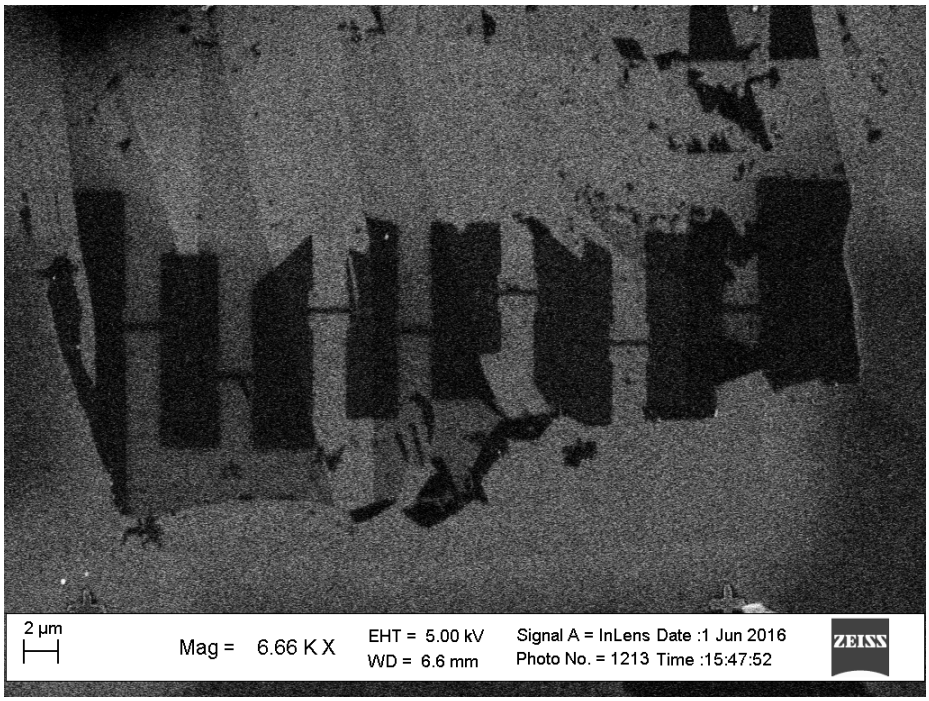

Figure 2.4: A SEM images of graphene from Figure 2.2 after ICP etching. It is etched to several nanoribbons.

2.4.4 Graphene Etching

We use inductively coupled plasma (ICP) to etch the exposed graphene. The recipe we use is to supply 50 sccm oxygen for 10 seconds under 15 mTorr pressure, 30 Watts forward power and 300 Watts ICP power.

10 seconds is usually long enough to etch up to few layers of graphene. We can use longer etching time to etch thicker graphene, however, too long etching time could dissolve PMMA and etch the graphene that is not supposed to be etched.

The unexposed PMMA is removed by an overnight 65 °C acetone bath followed by a IPA rinse. We can also anneal the wafer with oxygen at 350 °C to ensure complete removal of any resist residue.

2.5 Electrode Fabrication

To probe graphene properties electrically, we need to contact the graphene we find in the optical microscope with metallic electrodes. The pattern usually consists of small contacting electrodes and large bonding pads that connects to the measurement circuit. The fabrication process is shown in Figure 2.5.

2.5.1 Spin Coating

We use a bilayer of copolymer poly(methylmethacrylate-methacrylic acid) (MMA)/ PMMA. Both MMA and PMMA are spin coated at 1000 rpm/s ramp-up rate and 4000 rpm rotational speed, followed by hot plate baking at 150 °C and 180 °C for 10 minutes, respectively.

As opposed to the double PMMA layers used in section 2.4.2, we use MMA as the bottom layer. It's because MMA is more sensitive to e-beam exposure so we can produce an undercut in MMA. After depositing metal, it will act as an anchor point to prevent the metal to be lifted off.

2.5.2 Pattern Definition

There are usually two lithography methods people use to define patterns on resist, photo lithography and e-beam lithography. Photo lithography is good for rapid and large area patterns, but the fine structure size is limited by the light wavelength. We use e-beam lithography throughout this dissertation due to its high resolution.

The e-beam resist is exposed as the electron beam scans over the sample. We can

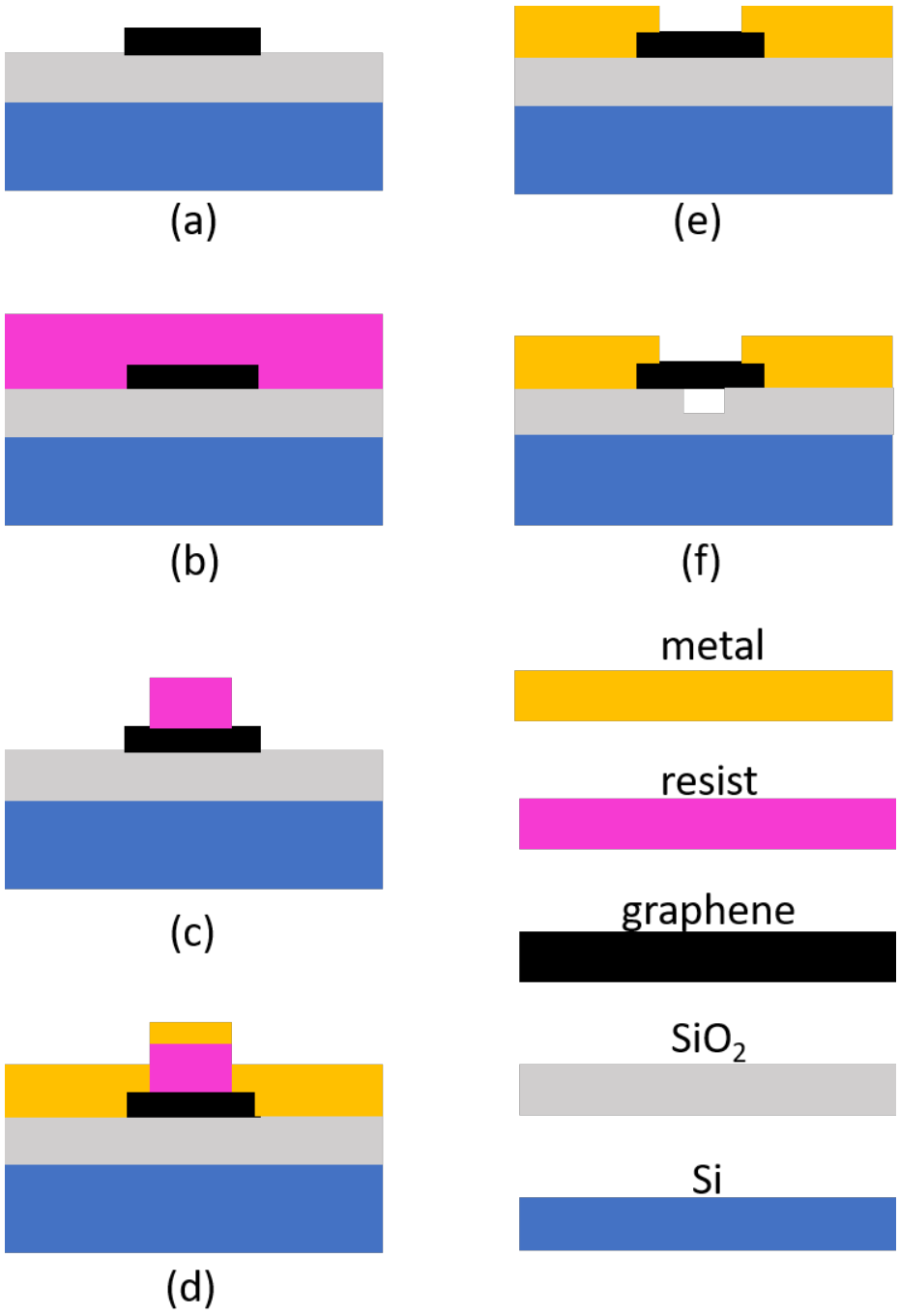

Figure 2.5: A schematic diagram of the fabrication process to create electrodes and suspend graphene. (a) Si/SiO_2 wafer with graphene on top. (b) Spin coat resist on the wafer. (c) Pattern the resist with e-beam lithography and develop to remove the exposed resist. (d) Deposit metal in evaporator. (e) Lift-off to remove the metal deposited on resist. The metal deposited on wafer stays. (f) Etch SiO_2 with buffered oxide etchant to suspend graphene.

Figure 2.6: The comparison between using PMMA/PMMA and MMA/PMMA as e-beam lithography resist layers. Since MMA is more sensitive to e-beam exposure, more MMA will be washed away after develop. The space will be filled up with metal after metal evaporation, and the extra metal in MMA will act as an anchor point to secure the metal to stay on the wafer.

determine the size and shape of the scanned area by importing a CAD file to the e-beam controlling software. Two types of e-beam resist is usually used in experiments, positive and negative resist. In the case of positive resist, the exposed resist will stay in developer and the unexposed resist will be washed away by the developer. Negative resist behaves in the opposite way. As a result, positive resist is often used when people want to expose a large area of wafer. In our experiments, we want to expose a small area of wafer for metal deposition, so negative e-beam resist is used in the experiment.

As mentioned above, the wafer is then developed in MIBK/IPA (1:3) solution for 70 seconds and rinsed in IPA for another 70 seconds to allow the exposed resist to be washed away. The wafer is then blown dry with nitrogen gas.

2.5.3 Metal Deposition

Gold is the most often used material for electrodes due to its high electrical conductivity. However, even with the anchor point created by MMA, the adhesion between gold and silicon dioxide is not strong enough to allow the metal to survive the following lift off step. We use a third material which is adhesive to both gold and silicon dioxide, while

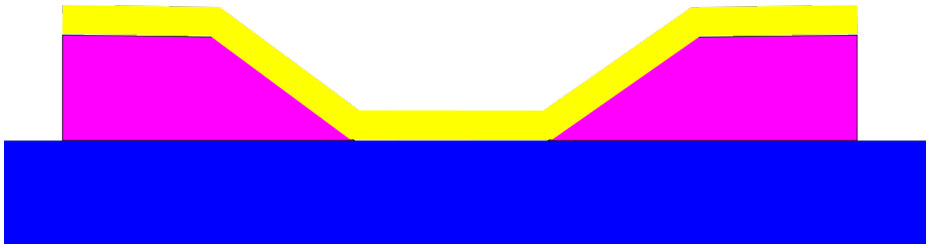

Figure 2.7: A schematic diagram of the wafer after metal deposition. Blue: SiO_2, pink: resist, yellow: metal. Metal in some areas is contacting the wafer, while in other areas is contacting the resist. The resist is resolved by acetone during lift-off, and the metal on the resist can be blown off. The metal contacting the wafer can stay in place after lift-off.

has relatively high electrical conductivity at the same time, as a "wetting layer". The most widely used wetting layer materials are chromium and titanium. The difference between these two is not crucial in our experiments.

We deposit a thin chromium layer (5 to 10 nm) at 1 Å/s followed by a 100 nm thick gold layer at 2 Å/s to the wafer.

2.5.4 Lift-off

As shown in Figure 2.7, the wafer is now completely covered with metal, with some areas contacting the wafer directly, some areas contacting the resist.

The purpose of lift-off is to remove the metal on the resist. The whole process needs to be done with the wafer completely submerged in acetone. To perform lift-off, we take the wafer out from the evaporator and put it directly in acetone, leave it overnight on a 65 °C hot plate. After resist is dissolved, blow the wafer carefully from the side through a pipette until the metal is completely detached from the wafer. Only until then the wafer can be taken out of acetone and rinsed with IPA.

2.6 Suspension

Graphene nanoribbons will not have mechanical motions when supported by substrate. In order to detect the mechanical resonance, we need to suspend the graphene nanoribbons.

A wet etching technique is introduced to etch SiO_2 in areas not protected by the metal electrodes. We put the wafer in the buffered oxide etchant to remove 120 nm thick SiO_2. It typically can be finished in 70 seconds. Now the graphene is clamped by metal electrodes and the SiO_2 underneath, while the SiO_2 between the electrodes are etched, forming a structure for the graphene to suspend. Then the sample is dried in a critical point dryer (CPD). The suspended graphene nanoribbon can easily break when leaving liquid environment because of liquid surface tension. Thus, the sample should be kept in liquid until it is transferred to the CPD chamber.

We use a small container to transfer the wafer to DI water and rinse the wafer 7 times. We then rinse the wafer in high quality IPA another 7 times. Now the wafer is ready to be placed in the CPD chamber.

Suspended graphene is much more fragile than substrate supported devices. After the sample is dried by CPD, it should be kept in a vacuum box to minimize the possibility of breaking.

Figure 2.8 and Figure 2.9(c) show SEM images of a suspended doubly clamped graphene nanoribbon and a suspended doubly clamped graphene sheet.

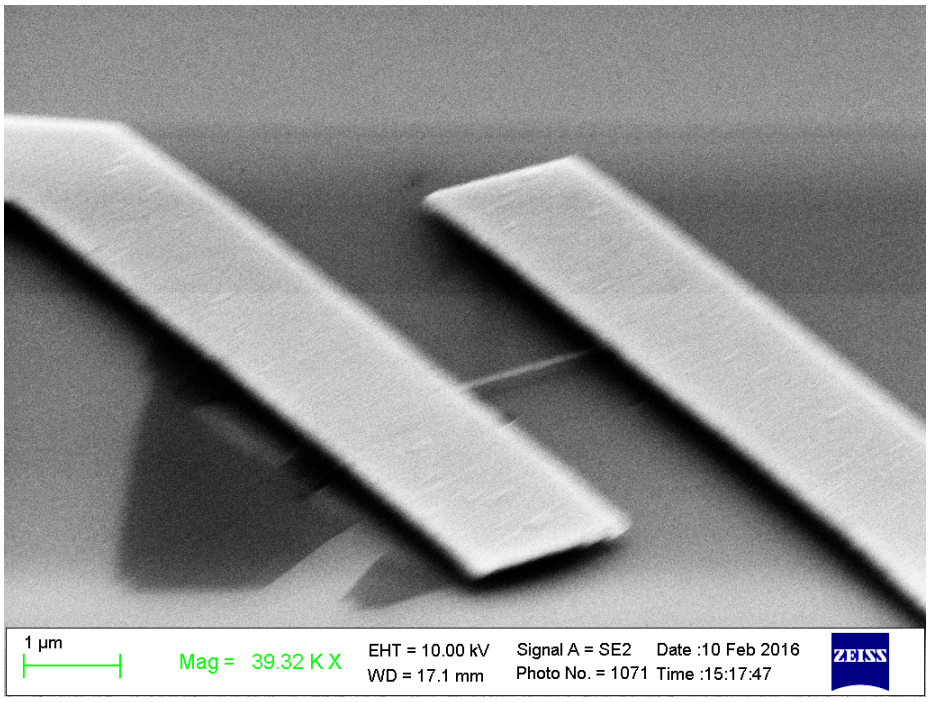

Figure 2.8: A SEM image of a suspended graphene nanoribbon.

2.7 Current Annealing

Compared to substrate supported devices, suspended devices are free from impurity and phonon scattering from the substrate, so people expect much higher mobility in those devices. Surprisingly, they don't show much difference until current annealing. It turns out the impurities that limit the transport performance of graphene are not coming from the substrate, but many are stuck on the graphene sheet. These impurities can be removed by driving a large current through the graphene sheet [5][34]. For unsuspended devices, the large current heats the graphene sheet locally to an estimated temperature of 600 °C and removes most of the residues remaining on the surface of graphene sheet from the previous fabrication steps. So current annealing has became a standard technique to remove the charge puddles and improve the device's response to the gate voltage. Literature reports up to ten fold mobility improvement can be achieved by current annealing [6].

Current annealing on suspended graphene must be performed in low temperatures, and the current must not exceed the break down current, which is reported as 1.6 mA/μm per graphene layer for exfoliated graphene [43]. In practice, to tolerate inaccurate graphene width measurement and non-perfect graphene quality, the maximum current is usually set to be much lower than the critical value. We set the maximum current value to be 0.2 mA/μm per graphene layer. In each current annealing cycle, we slowly increase the current through the graphene sheet to 0.1 mA/μm, 0.12 mA/μm, 0.14 mA/μm, 0.16 mA/μm, 0.18 mA/μm and 0.2 mA/μm, respectively, wait for several minutes and decrease the current to zero. We check the gate response after each cycle. The procedure is applied repeatedly until the gate response signal changes.

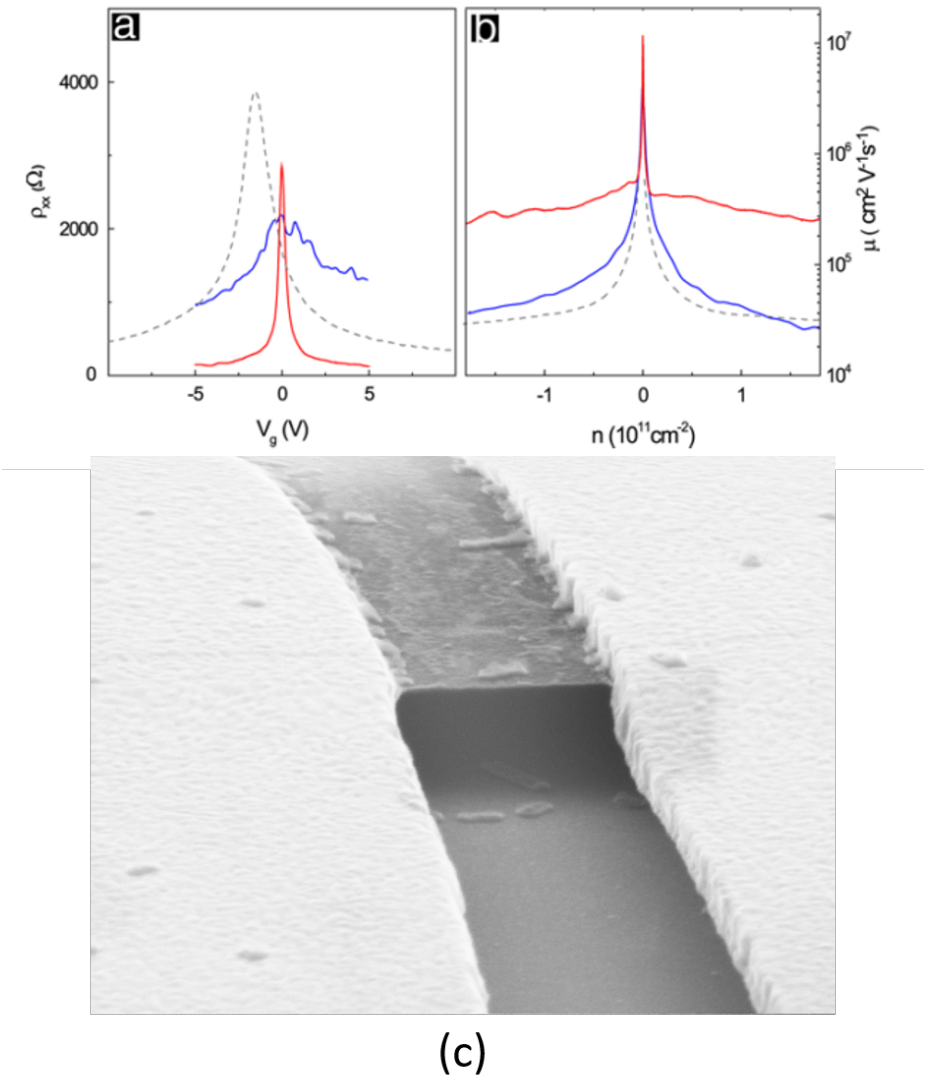

Figure 2.9: A SEM image of a typical suspended graphene sheet before current annealing and transport properties before and after current annealing. (a) Measured four-probe resistivity ρ_{xx} as a function of gate voltage V_g for a device before (blue) and after (red) current annealing. Data from a traditional high-mobility device on the substrate (gray dotted line) shown for comparison. (b) Mobility μ as a function of carrier density n for the same device. (c) Impurities can be clearly seen on the surface of suspended graphene sheet. Figure (a)(b) are adopted from [6].

Chapter 3

Shadow Mask

3.1 Introduction

In the last chapter, we discussed the fabrication techniques used to make most of the devices worldwide. Graphene devices usually contain only one or a few layers of carbon atoms, as a result, they are sensitive to external contaminations. while the e-beam lithography has a high resolution and been proven to be a robust method, it introduces polymers and chemical fluids, including resist residues to the devices, and it will modify graphene's electrochemical potential and generate extra charge puddles. To improve device quality, people often use thermal annealing and current annealing. However, at the same time, people have to live with the risk of burning the device to break.

In this chapter, we introduce a lithography-free fabrication technique, shadow mask technique. It is a simple and inexpensive technique which requires metal evaporation through a pre-defined silicon mask. In the whole process, the graphene device doesn't contact any resist or chemical fluid. Once the shadow mask is made, it can be re-used for

over 50 times. Since metal evaporation is already one of the steps in the standard e-beam lithography method, so overall, the shadow mask technique increases device throughput and fabrication speed. Using this technique, people fabricated both substrate-supported and suspended devices [1][2].

3.2 Mask Fabrication

The shadow mask is a piece of patterned silicon wafer. The general idea of the mask fabrication is to define a pattern on a piece of hard wafer, then transfer the pattern to the wafer. The approach we take is to define a pattern on a polymer resist layer by e-beam lithography, and use the resist layer as a mask to tranfer the pattern to chromium layer which is pre-deposited on a silicon wafer, then use the chromium layer as a mask to etch the silicon wafer so that the pattern is transferred to the silicon wafer.

3.2.1 Silicon Wafer

Mask patterns are defined on hard wafers. The wafers need to be easy to cut to small pieces and easy to etch. They also need to be high in strength, Young's modulus, flexural modulus, shear modulus, high in thermal conductivity, chemical inert and low in thermal expansion to ensure the masks are robust to use and hard to deform during experiment, so that patterns do not shift or distort when metal is evaporated through shadow masks. Here we use 300 μm thick, single-side-polished, {100} orientation silicon wafers. Note the wafer we use here doesn't contain an oxide layer.

To prepare the shadow masks, we cut the wafer into about 1 cm $\times$ 1.5 cm pieces

(larger than the wafer size we use for graphene samples), clean the wafer thoroughly with acetone and rinse it with IPA and deionized water (DI water).

3.2.2 Pattern Definition

1. Chromium deposition.

A 200 nm layer of chromium is evaporated on the polished side of the silicon wafer. If the chromium layer is too thick, it will be hard to transfer the pattern. Also, as the chromium etching time becomes longer, the pattern on the chromium mask will diffuse. On the other hand, if the chromium layer is too thin, it will crack easily and will not survive the later ICP etching step.

2. PMMA spin coating.

Two PMMA layers are spun on top of the chromium layer. We use a rotational speed of 4000 rpm and a ramp-up rate of 1000 rpm/s to make each layer 180 nm thick. Wafer is baked at 180 °C for 10 minutes after spinning coat each PMMA layer.

3. Pattern definition.

The wafer is placed in a scanning electron microscope to define the pattern on PMMA with e-beam lithography. The electrodes are usually made no narrower than 1 μm to ensure the plasma can go through the chromium pattern during the later ICP etching step. The electrodes features also need to avoid sharp corners to minimize the cracking possibilities of the chromium mask. The e-beam exposed PMMA resist is then developed in MIBK/IPA (1:3) solution for 65 seconds.

3.2.3 Etching

1. Chromium etching.

Now the pattern is in the PMMA layer. We use the pattern on PMMA layer as a mask to etch chromium. We soak the wafer in chromium etchant for about 90 seconds. The exact time depends on the etchant quality and it can vary from sample to sample. We need to take the wafer out of the etchant and check if the chromium is etched completely frequently. The chromium layer should not be over-etched, otherwise the pattern will blur in the chromium layer and significantly affect the device quality. Then the wafer is soaked in acetone at 65 °C for 30 minutes to completely remove PMMA.

2. Silicon etching.

The wafer is then placed in inductively coupled plasma (ICP) system and the chromium layer is used as a mask to transfer the pattern to the silicon wafer. It is etched by several cycles of SF_6 and C_4F_8. In each cycle, we inject 70 sccm SF_6 for 8 seconds under 25 mTorr pressure, 50 W forward power and 450 W ICP power, followed by 50 sccm C_4F_8 for 6 seconds under 30 mTorr pressure, 20 W forward power and 400 W ICP power.

The chromium layer is not durable under long plasma etching times. We first use thermal tapes to expose a square window on the back of the wafer and etch the silicon from the back. The window need to cover the pattern area on the front. However, too large window size will leave too small portion of the wafer un-etched and leave the whole wafer unsupported. We usually use the tape to cover at least 0.5 cm on each wafer edge to ensure good support.

We use a Dektak Surface Profilometer to examine the etched thickness and etch

the silicon wafer from back until about 50 μm is left. Then we flip the wafer and etch it from the front. The chromium mask protects the wafer and only the pattern part is etched. The chromium mask is very fragile to plasma etching so the etching is divided into small cycles, usually 30 seconds, to prevent over-etching. The mask is finished when the pattern is completely etched through.

The yield of the shadow mask fabrication can reach 70% if each step is conducted carefully.

3.3 Mask Usage

Even though fabricating shadow masks themselves involves lithography and etching, using them to fabricate devices is totally lithography free and can be quickly done. We simply align the shadow mask to the desired location on the sample and evaporate metal onto the sample surface through the mask.

We use a three-axis stage, shown in Figure 3.3, to secure the shadow mask and the sample to achieve perfect alignment. The shadow mask is clamped on the top of the side pillar of the stage with the chromium side facing down. The sample is put on a electrical tape glued to the top of the stage main body. The X, Y and Z knobs are turned to achieve good alignment and contact between the shadow mask and the sample. Sometimes it's helpful to etch alignment windows in addition to the real pattern to allow better look through and result in a better alignment.

The stage is then put in the evaporator upside down to allow metal to be evapo-

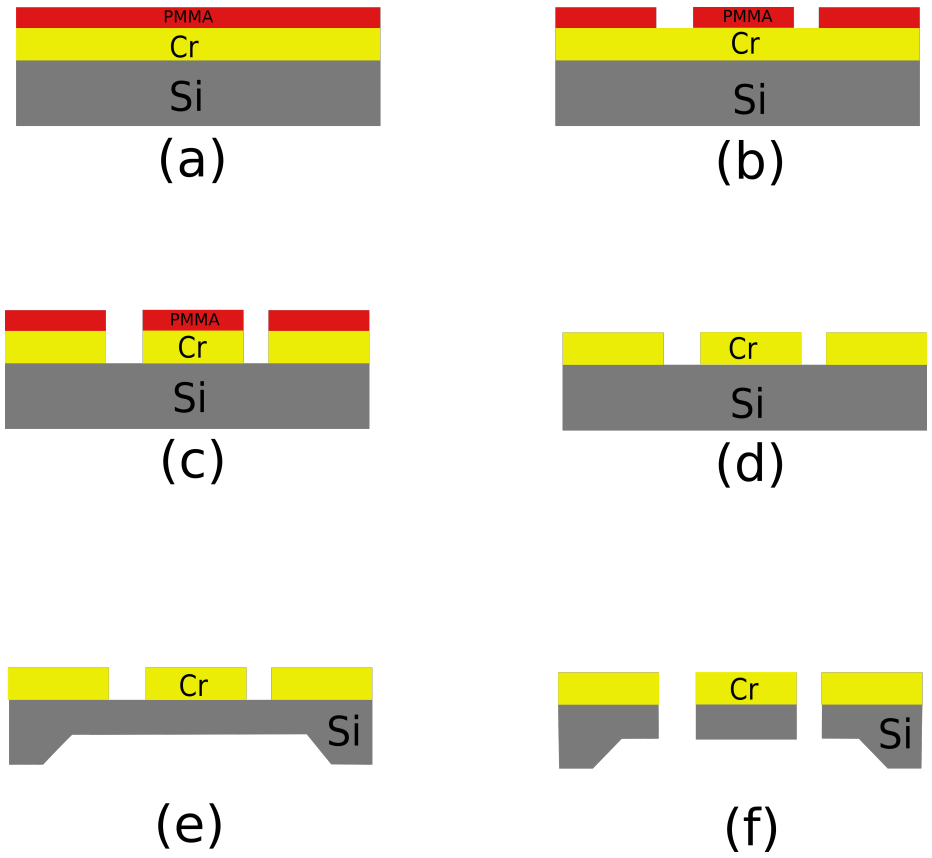

Figure 3.1: A schematic diagram of the fabrication process of shadow masks. (a) Deposit 200nm chromium layer on top of a piece of Si wafer(no silicon dioxide layer), then spin coat two layers of PMMA on top of chromium. (b) Use E-beam lithography to define the desired pattern in PMMA, then develop to wash away the exposed PMMA. (c) Soak the wafer in chromium etchant to etch the exposed chromium. (d) Remove PMMA in acetone bath. (e) Use thermal tape to define a window on the back of the wafer and etch the exposed silicon using ICP. (f) Etch the wafer from the front. Chromium mask protects the un-patterned silicon.

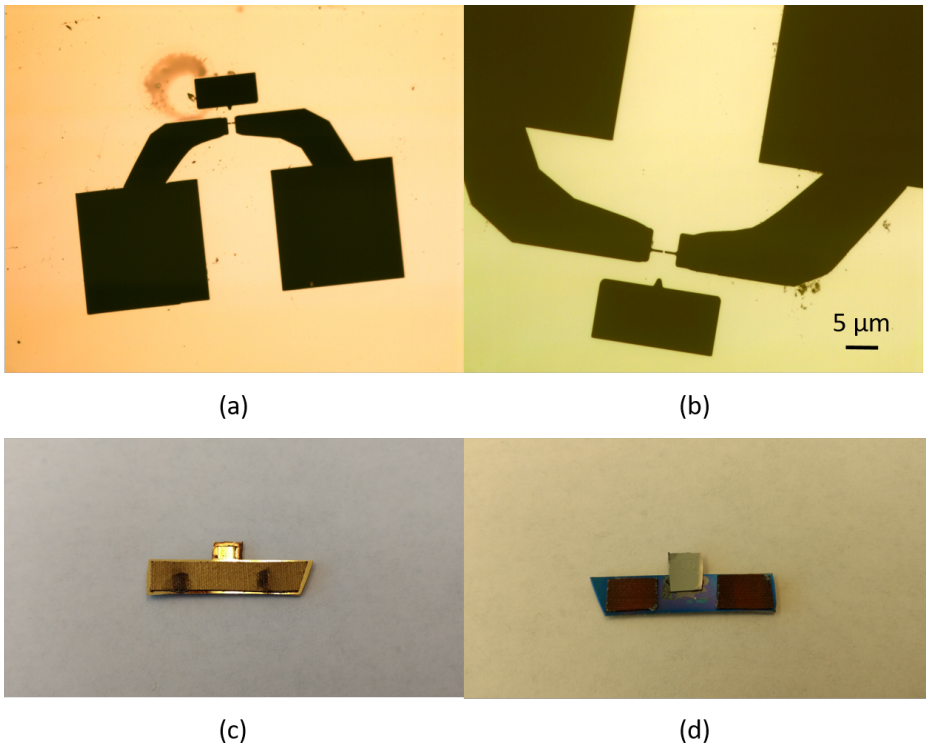

Figure 3.2: Pictures of finished shadow masks. (a)Optical microscope images of finished shadow mask. The wide electrodes, extra square opening on the top and the tip on the bottom side of the square help to provide better view through the mask and can results in a better alignment. (b) A zoom in view of the electrodes in (a). (c)(d) Front and back views of a finished mask after being installed to a bar wafer.

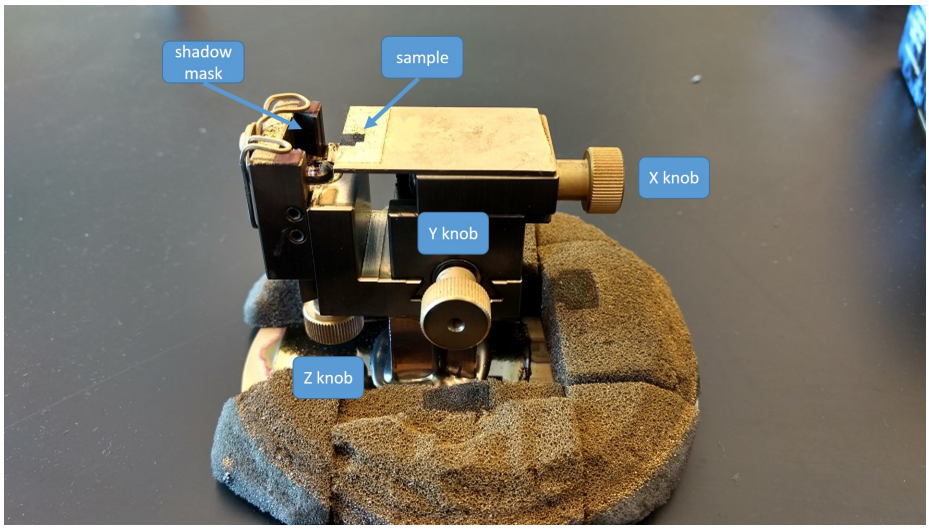

Figure 3.3: A side view of the alignment stage. Shadow mask is clamped on the top of the stage pillar. Sample wafer is placed on the top of the stage main body. After installing the mask and the sample wafer, X, Y and Z knobs are tuned to achieve good alignment and contact between the shadow mask and the sample wafer.

rated through the mask and land on the graphene wafer.

The relative position between the evaporation mask and the sample wafer is crucial for determining where the pattern is deposited. In traditional fabrication method, we use developed photo resist or e-beam resist as the mask. Because the resist is spin-coated on the wafer, the relative position is fixed. While shadow mask is clamped on the stage, and the relative position to the sample wafer can change, so extra care has to be taken to better secure them. We glue padding foams on the stage base to provide cushion between the stage and the evaporator sample holder. When evaporating metal in traditional methods, we often rotate the evaporator sample holder to achieve uniform evaporated metal surface. However, we need to turn this function off when using shadow masks to eliminate abrupt motions which could cause the relative position to change. We also glue sand paper on both stage and the wafer bar at the mask clamping point to provide greater friction. The

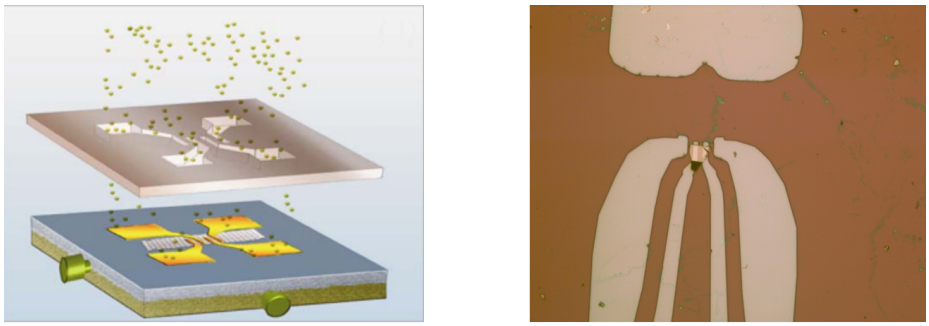

Figure 3.4: Usage of shadow masks and a optical image of finished devices. (a) Graphene devices can be fabricated by direct deposition of metallic electrodes through shadow masks [2]. (b) An example of finished devices. Figure (a) is adapted from paper [2]

electrical tape which holds the sample wafer needs to be replaced every few depositions. Overall, careful handling during the whole process will both secure the relative position and protect the shadow mask from breaking.

Though taking special cares can improve alignment accuracy dramatically, it's still inevitable due to mechanical motions and thermal expansions. We usually use it when alignment accuracy is not crucial or it's larger than 1 μm and the desired pattern size is larger than 200 nm. With careful handling, a shadow mask can be re-used by more than 50 times.

3.4 Conclusion

Shadow mask technique has been proven to be a clean, fast and robust technique to fabricate both wafer supported and suspended devices on various two-dimensional materials [1][2]. We successfully fabricated various devices with pattern as small as 200 nm and achieved alignment accuracy up to 1 μm.

Chapter 4

Measurement Techniques and Setup

4.1 Introduction

To study the resonating system, we need to induce and detect their mechanical motion. Among various techniques, the essential idea is the same – we introduce an oscillating force on the device, and tune the frequency to be the same as the intrinsic resonance frequency of the device, we then either detect the mechanical motion directly or detect a converted low frequency signal. The often used actuation techniques include peizo induced oscillation [27], magnetic actuation [10][18], electrostatic actuation [11][12], thermal fluctuation induced resonance [4] and optical actuation [19]. The detection can also be carried out with various techniques, for example, optical imaging [15][39], magnetomotive [10][41], electrostatic [33] and piezoelectric methods [3].

Each actuation and detection has its own advantages and disadvantages. For example, electrostatic method requires small current but high voltage, magnetomotive method requires a small voltage but a high magnetic field, and piezoelectric method requires a sophisticated piezo stage and a very stable base station. After careful consideration, we decided to use the electrostatic actuation and detection technique due to its simplicity and high accuracy in measuring signals. At the same time, it allows us to explore the field-effect transistor properties, which is an exceptional and interesting phenomenon in graphene devices. However, the resistance in graphene devices is not fixed due to fabrication process and field effect, and it's usually much higher than the typical transmission line impedance of 50 Ω. We need to overcome the impedance mismatch to minimize the signal loss. We analyze the system following closely to Dr. Tengfei Miao [32] and Dr. Hsin-Ying Chiu's [8] dissertations.

4.2 Electrical Actuation

The graphene nanoribbon resonator system we work with is shown in Figure 4.1. A capacitor is formed by the graphene plane and the back gate. So we can approach the system in a classical parallel plane capacitor method. By varying the back gate voltage, we can tune the electrical field between the gate and the graphene. When a current is flowing through the graphene device, the change of electrical field results in a change in electrical force on graphene. Therefore, the graphene is actuated, and a resonance can be excited when the gate voltage is varied at the resonance frequency.

To find the driving force in electrostatic system, we derive starting with the energy

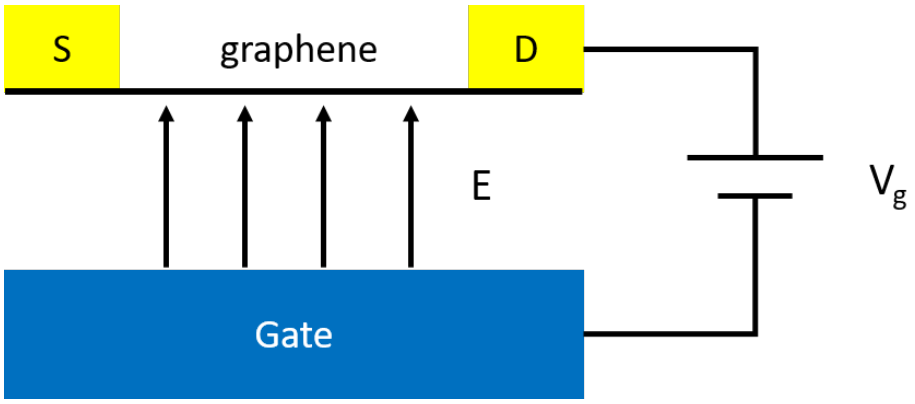

Figure 4.1: A schematic diagram of the graphene nanoribbon resonator system as a parallel plate capacitor. The graphene and the back gate forms a parallel plate capacitor.

in the system. To move a unit charge dq to the plate at voltage V_g, the elementary energy is

$$dU_s = V_g dq = \frac{q}{C} dq \tag{4.1}$$

where U_s is the energy in the system, q is the charge and C is the capacitance. To find the total system energy with charge Q, we integrate q from 0 to Q.

$$U_s = \int_0^Q \frac{q}{C} dq = \frac{1}{2}\frac{Q^2}{C} = \frac{1}{2} C V_g^2 \tag{4.2}$$

With gate voltage V_g, the charge on graphene is

$$Q = -CV_g \tag{4.3}$$

If we fix the gate voltage V_g and change the distance from graphene to back gate by dz, the electrostatic energy change is

$$dU_s = \frac{1}{2} dC V_g^2 \tag{4.4}$$

and the work done by the battery is

$$dU_b = V_g dQ = -dC V_g^2 \tag{4.5}$$

Combine equation 4.4 and equation 4.5, we find the total energy change in the system if we change the distance by dz

$$dU = dU_s + dU_b = -\frac{1}{2}dCV_g^2 \tag{4.6}$$

The electrostatic force on the graphene can be easily found by take the derivative.

$$F_{es} = -\frac{dU}{dz} = \frac{1}{2}\frac{dC}{dz}V_g^2 \tag{4.7}$$

The resonance is actuated when there is AC current flowing across the graphene sheet. The source-drain bias voltage we apply contains a DC component V_{sd} and an AC component $\tilde{V_{sd}}$. The effective potential on graphene is half of the source-drain voltage. So the electrostatic force becomes

$$F_{es} = \frac{1}{2}\frac{dC}{dz}[V_g - \frac{1}{2}(V_{sd} + \tilde{V}_{sd})]^2 \tag{4.8}$$

we can omit V_{sd} if it's small compared to V_g. So we find the final expression for electrostatic force

$$F_{es} = \frac{1}{2}\frac{dC}{dz}(V_g - \frac{1}{2}\tilde{V}_{sd})^2 \tag{4.9}$$

and the ac driving force

$$\tilde{F}_{es} = -\frac{1}{2}\frac{dC}{dz}V_g\tilde{V}_{sd} \tag{4.10}$$

4.3 Electrical Readout

As we know, the modulation in graphene conductance can be tuned by a modulation in charge density in graphene,

$$\tilde{G} = \frac{dG}{dq}\tilde{q} \tag{4.11}$$

and charge density can be tuned by capacitance.

$$\tilde{q} = \tilde{C} V_g \tag{4.12}$$

So if the graphene nanoribbon oscillates, it will cause a change in the conductance. We can notice the change by measuring the current.

Suppose the distance between the graphene sheet and the back gate is z. It oscillates with amplitude δz and frequency ω.

$$z = z_0 + \delta z(\omega) \tag{4.13}$$

Where z_0 is the equilibrium distance. Perform a Taylor expansion on conductance at z_0. We find the modulated conductance is

$$\tilde{C} = C' \delta z(\omega) \tag{4.14}$$

Inserting equation 4.14 into equation 4.12, then into equation 4.11, we get

$$\tilde{G} = \frac{dG}{dq} C' \delta z(\omega) V_g \tag{4.15}$$

Therefore, the conductance is tuned at frequency ω. Because the mechanical motion is driven by external force, the displacement frequency is the same as the force frequency. From equation 4.10 we know the force is induced by $\tilde{V}_{sd}$, force frequency is the same as $\tilde{V}_{sd}$ frequency. Therefore, the frequency of modulated conductance equals the frequency of ac bias voltage.

In this dissertation, we mainly study the mechanical motion on a monolayer graphene nanoribbon of 0.2 μm wide and 2 μm long. The resonance frequency of the

fundamental mode is typically 100 MHz $\sim$ 200 MHz. Direct detection of such a high frequency signal is challenging due to impedance mismatch and parasitic capacitance. And a highly dedicated matching circuit is often required. However, high frequency signals can also be detected indirectly through signal mixing. We can use a mixer to convert a high frequency signal to a low frequency signal without losing information about its amplitude. As a result, the detection circuit can be kept simple, robust and low cost. This technique successfully detects NEMS signals on various geometries and materials [9][13][20][22][33][37].

In the following sections, we introduce two types of one source mixing techniques, amplitude modulation (AM) and frequency modulation (FM). In both cases, we use ω to represent resonance frequency, which is on the order of 100 MHz, and ω_L to represent the low frequency we mix with high frequency. ω_L is the target frequency we want to measure.

4.4 Amplitude Modulation

In the amplitude modulation (AM) technique, we apply an AM signal as the source drain bias voltage. The amplitude of V_{sd} is modulated by an amplitude of A at frequency ω_L

$$\tilde{V}_{sd} = V_{sd}[1 + A\cos(\omega_L t)]\cos(\omega t) \tag{4.16}$$

where A is the modulation amplitude. We assume it to be 100% for simplicity. Inserting it into equation 4.10, we get the ac driving force to be

$$\tilde{F} = -\frac{1}{2}C'V_gV_{sd}[1 + \cos(\omega_L t)]cos(\omega t) \tag{4.17}$$

Inserting it into 1.18, we find

$$\tilde{z} = \delta z(\omega)[1 + \cos(\omega_L t)]\cos(\omega t + \phi_M) \tag{4.18}$$

where the vibration amplitude

$$\delta z(\omega) = \frac{-C' V_g V_s d/2m}{\sqrt{(\omega_0^2 - \omega^2)^2 + (\omega\omega_0/Q)^2}} \tag{4.19}$$

and ϕ_M is the phase of mechanical response relative to the drive.

The total displacement can be expressed as

$$z = z_0 + \delta z \tag{4.20}$$

with $z_0 \neq 0$ due to the electrostatic bending toward the gate induced by V_g

The current flowing through graphene is a function of bias voltage V_{sd} and the displacement z. We perform a Taylor expansion on $I(V_{sd}, z)$ at $V_{sd} = 0$ and $z = z_0$.

$$\begin{aligned} I(V_{sd}, z) =& I(V_{sd} = 0, z = z_0) \\ &+ \frac{\partial I}{\partial V_{sd}}\tilde{V}_{sd} + \frac{\partial I}{\partial z}\tilde{z} \\ &+ \frac{1}{2}\frac{\partial^2 I}{\partial V_{sd}^2}\tilde{V}_{sd}^2 + \frac{\partial^2 I}{\partial V_{sd}\partial z}\tilde{V}_{sd}\tilde{z} + \frac{1}{2}\frac{\partial^2 I}{\partial^2 z}\tilde{z}^2 \end{aligned} \tag{4.21}$$

In the above formula, the low frequency term $\cos(\omega_L t)$ in $\tilde{V}_{sd}$ and $\tilde{z}$ cannot be singled out, so they will not be picked up by the low frequency detection circuit. We can safely neglect the first order terms $\frac{\partial I}{\partial V_{sd}}\tilde{V}_{sd}$ and $\frac{\partial I}{\partial z}\tilde{z}$.

The current does not exist when there is no source-drain voltage. So the zero order term $I(V_{sd} = 0, z = 0)$ and $\frac{1}{2}\frac{\partial^2 I}{\partial^2 z}\tilde{z}^2$ can also be neglected.

Let's take a close look at the remaining two terms $\frac{1}{2}\frac{\partial^2 I}{\partial V_{sd}^2}\tilde{V}_{sd}^2$ and $\frac{\partial^2 I}{\partial V_{sd}\partial z}\tilde{V}_{sd}\tilde{z}$.

$$\begin{aligned}\frac{1}{2}\frac{\partial^2 I}{\partial V_{sd}^2}\tilde{V}_{sd}^2 &= \frac{1}{2}\frac{\partial^2 I}{\partial V_{sd}^2}V_{sd}^2[1+cos(\omega_L t)]^2\cos^2(\omega t) \\ &= \frac{1}{2}\frac{\partial^2 I}{\partial V_{sd}^2}V_{sd}^2[1+2\cos(\omega_L t)+\cos^2(\omega_L t)]\frac{1}{2}[1+\cos(2\omega t)]\end{aligned} \tag{4.22}$$

The low frequency component is

$$I_{\omega_L}^{(1)} = \frac{1}{2}\frac{\partial^2 I}{\partial V_{sd}^2}V_{sd}^2\cos(\omega_L t) \tag{4.23}$$

and

$$\begin{aligned}\frac{\partial^2 I}{\partial V_{sd}\partial z}\tilde{V}_{sd}\tilde{z} &= \frac{\partial^2 I}{\partial V_{sd}\partial z}V_{sd}[1+\cos(\omega_L t)]\cos(\omega t)\delta z[1+\cos(\omega_L t)]\cos(\omega t+\phi_M) \\ &= \frac{\partial^2 I}{\partial V_{sd}\partial z}V_{sd}\delta z[1+\cos(\omega_L t)]^2\cos(\omega t)\cos(\omega t+\phi_M) \\ &= \frac{\partial^2 I}{\partial V_{sd}\partial z}V_{sd}\delta z[1+2\cos(\omega_L t)+\cos^2(\omega_L t)]\frac{1}{2}[\cos(\phi_M)+\cos(2\omega t+\phi_M)]\end{aligned} \tag{4.24}$$

The low frequency component is

$$I_{\omega_L}^{(2)} = \frac{\partial^2 I}{\partial V_{sd}\partial z}V_{sd}\delta z\cos(\omega_L t)\cos(\phi_M) \tag{4.25}$$

The total low frequency mixing current is

$$I_{\omega_L}^{AM} = I_{\omega_L}^{(1)} + I_{\omega_L}^{(2)} \tag{4.26}$$

Among the total low frequency current, $I_{\omega_L}^{(1)}$ is the background signal and $I_{\omega_L}^{(2)}$ is due to the mechanical motion.

4.5 Frequency Modulation

In frequency modulation (FM) technique, we instead apply a FM signal as the source drain bias voltage. We follow paper [17] to derive the theory. The instantaneous

frequency ω_i is modulated by an amplitude of ω_Δ, in frequency ω_L

$$\omega_i = \omega_c + \omega_\Delta \cos(\omega_L t) \tag{4.27}$$

where ω_c is the carrier frequency. Usually $\omega_c \gg \omega_\Delta \gg \omega_L$. Integrate ω_i over time, we find the instantaneous phase to be

$$\phi_i(t) = \omega_c t + \frac{\omega_\Delta}{\omega_L} sin(\omega_L t) \tag{4.28}$$

therefore, the expression for bias voltage is

$$\tilde{V}_{sd} = V_{sd} \cos[\omega_c t + \frac{\omega_\Delta}{\omega_L} \sin(\omega_L t)] \tag{4.29}$$

We adopt the same analytical approach and perform a Taylor expansion on current I like equation 4.21

$$\begin{aligned} I(V_{sd}, z) =& I(0, z_0) \\ &+ \frac{\partial I}{\partial V_{sd}} \tilde{V}_{sd} + \frac{\partial I}{\partial z} \tilde{z} \\ &+ \frac{1}{2} \frac{\partial^2 I}{\partial V_{sd}^2} \tilde{V}_{sd}^2 + \frac{\partial^2 I}{\partial V_{sd} \partial z} \tilde{V}_{sd} \tilde{z} + \frac{1}{2} \frac{\partial^2 I}{\partial^2 z} \tilde{z}^2 \end{aligned} \tag{4.30}$$

Out of the same reason as before, there is no current when in the absence of source-drain voltage, so

$$\begin{aligned} I(0, z_0) &= 0 \\ \frac{\partial I}{\partial z} \tilde{z} &= 0 \\ \frac{1}{2} \frac{\partial^2 I}{\partial^2 z} \tilde{z}^2 &= 0 \end{aligned} \tag{4.31}$$

and $\frac{\partial I}{\partial V_{sd}} \tilde{V}_{sd}$ gives only high frequency signal.

Let's take a close look at the remaining terms $\frac{1}{2}\frac{\partial^2 I}{\partial V_{sd}^2}\tilde{V}_{sd}^2$ and $\frac{\partial^2 I}{\partial V_{sd}\partial z}\tilde{V}_{sd}\tilde{z}$. It's useful to decompose the applied FM signal with Jacobi-Anger expansion:

$$\begin{aligned}\tilde{V}_{sd} &= V_{sd} \times [J_0(\frac{\omega_\Delta}{\omega_L})\cos(\omega_c t) + \sum_{n=1}^{\infty} J_n(\frac{\omega_\Delta}{\omega_L})(\cos((\omega_c - n\omega_L)t) + (-1)^n \cos((\omega_c + n\omega_L)t))] \\ &= V_{sd} \times [J_0(\frac{\omega_\Delta}{\omega_L})\cos(\omega_c t) + \sum_{n=odd} J_n(\frac{\omega_\Delta}{\omega_L}) 2\sin(\omega_c t)\sin(n\omega_L t) \\ &+ \sum_{n=even} J_n(\frac{\omega_\Delta}{\omega_L}) 2\cos(\omega_c t)\cos(n\omega_L t)]\end{aligned} \tag{4.32}$$

V_{sd} is a constant, so we only need to look at the terms in the parenthesis. We use V_k to represent the k-th order expansion term and A_k to represent the constant coefficient in that term. To find the low frequency terms in $\tilde{V}_{sd}^2$, we first look at the square terms.

When $k = 0$,

$$V_{0,0} = J_0^2(\frac{\omega_\Delta}{\omega_L})\cos^2(\omega_c t) \tag{4.33}$$

There is no ω_L terms.

When k = odd

$$\begin{aligned}V_{k,k} &= A_{k,k}\sin^2(\omega_c t)\sin^2(k\omega_L t) \\ &= A_{k,k}\frac{1-\cos(2\omega_c t)}{2}\frac{1-\cos(2k\omega_L t)}{2}\end{aligned} \tag{4.34}$$

When k = even

$$\begin{aligned}V_{k,k} &= A_{k,k}\cos^2(\omega_c t)\cos^2(k\omega_L t) \\ &= A_{k,k}\frac{1+\cos(2\omega_c t)}{2}\frac{1+\cos(2k\omega_L t)}{2}\end{aligned} \tag{4.35}$$

Since k is an integer, the lowest frequency term we can get is $\cos(2\omega_L t)$. So there is no low frequency signal from these terms.

We then look at the cross terms. Clearly, the $\cos(\omega_L t)$ term can only be produced by the cross multiplication of two adjacent expansion terms, so we only need to examine $V_{k,k-1}$. First let $k = 1$

$$\begin{aligned} V_{0,1} &= A_{0,1}\cos(\omega_c t)[\cos(\omega_c t - \omega_L t) - \cos(\omega_c t + \omega_L t)] \\ &= A_{0,1}[\frac{\cos(2\omega_c t - \omega_L t) + \cos(\omega_c t)}{2} - \frac{\cos(2\omega_c t + \omega_L t) + \cos(\omega_c t)}{2}] \end{aligned} \tag{4.36}$$

We then write out the expression for $V_{k,k-1}$ when $k \neq 1$. Without losing generality, let k be even.

$$\begin{aligned} \frac{V_{k,k-1}}{A_{k,1}} &= [\cos(\omega_c t - k\omega_L t) + \cos(\omega_c t + k\omega_L t)][\cos(\omega_c t - (k-1)\omega_L t) - \cos(\omega_c t + (k-1)\omega_L t)] \\ &= \cos(\omega_c t - k\omega_L t)\cos(\omega_c t - (k-1)\omega_L t) - \cos(\omega_c t - k\omega_L t)\cos(\omega_c t + (k-1)\omega_L t) \\ &+ \cos(\omega_c t + k\omega_L t)\cos(\omega_c t - (k-1)\omega_L t) - \cos(\omega_c t + k\omega_L t)\cos(\omega_c t + (k-1)\omega_L t) \\ &= \frac{\cos(2\omega_c t - (2k-1)\omega_L t) + \cos(\omega_L t)}{2} - \frac{\cos(2\omega_c t - \omega_L t) + \cos(\omega_L t)}{2} \\ &+ \frac{\cos(2\omega_c t - \omega_L t) + \cos(\omega_L t)}{2} - \frac{\cos(2\omega_c t + (2k-1)\omega_L t) + \cos(\omega_L t)}{2} \end{aligned} \tag{4.37}$$

Clearly, $\cos(\omega_L t)$ terms cancels each other in both cases. Together with the square terms, we conclude there is no low frequency contribution from $\frac{1}{2}\frac{\partial^2 I}{\partial V_{sd}^2}\tilde{V}_{sd}^2$.

Now let's take a look at $\frac{\partial^2 I}{\partial V_{sd}\partial z}\tilde{V}_{sd}\tilde{z}$. Remember equation 4.29

$$\tilde{V}_{sd} = V_{sd}\cos[\phi(t)] \tag{4.38}$$

$$\phi(t) = [\omega_c t + \frac{\omega_\Delta}{\omega_L}\sin(\omega_L t)] \tag{4.39}$$

and equation 4.10

$$\tilde{F} = -\frac{1}{2}C' V_g \tilde{V}_{sd} \tag{4.40}$$

We'd like to Taylor expand $\phi(t + \Delta t)$. The time interval Δt we are interested in is of the order or smaller than the timescale of the oscillator Q/ω_0, where Q is the quality factor of the resonator. If the oscillation frequency is much larger than the modulation magnitude, i.e. $\omega_c \gg \omega_\Delta$, we can safely ignore the higher order terms. If the oscillation timescale is much smaller than the modulation timescale, i.e. $\omega_0/Q \gg \omega_L$, we can again ignore the transient oscillation. The electromechanical current is only significant at the resonant frequency ω_0 so approximately we consider $\omega_c \approx \omega_0$. In experiment, the typical values are:

$$\omega_c \sim 100MHz$$

$$\omega_\Delta = 100KHz$$

$$\omega_L \sim 1KHz$$

The above requirements are easily met. So we expand $\phi(t + \Delta t)$

$$\phi(t + \Delta t) = \phi(t) + \omega_i \Delta t \tag{4.41}$$

where $\phi(t)$ is a constant, and the instantaneous frequency

$$\omega_i = \frac{\partial \phi}{\partial t} = \omega_c + \omega_\Delta \cos(\omega_L t) \tag{4.42}$$

so

$$\tilde{V}_{sd} = V_{sd} \cos[\phi(t) + \omega_i \Delta t] \tag{4.43}$$

$$\tilde{F} = F_0 \cos[\phi(t) + \omega_i \Delta t] \tag{4.44}$$

where

$$F_0 = -\frac{1}{2} C' V_g V_{sd} \tag{4.45}$$

Inserting $\tilde{F}$ into equation 1.18, we get

$$\tilde{z} = \delta z \cos[\phi(t) + \omega_i \Delta t + \phi_M] \tag{4.46}$$

where δz is the displacement magnitude and ϕ_M is the phase delay of mechanical response relative to the drive. Therefore,

$$\begin{aligned} \tilde{z}\tilde{V}_{sd} &= \delta z \cos[\phi(t) + \omega_i \Delta t + \phi_M] V_{sd} \cos[\phi(t) + \omega_i \Delta t] \\ &= \frac{1}{2}\delta z V_{sd}[\cos(\phi_M) + \cos(2\omega_i \Delta t + 2\phi(t) + \phi_M)] \\ &= \frac{1}{2} Re(\delta^* z) V_{sd} + \frac{1}{2}\delta z V_{sd} \cos[2\omega_i \Delta t + 2\phi(t) + \phi_M] \end{aligned} \tag{4.47}$$

where $\delta^* z$ is the complex displacement.

$$\delta z^* = \delta z[\cos(\phi_M) + i \sin(\phi_M)] \tag{4.48}$$

The second term in $\tilde{z}\tilde{V}_{sd}$ contains high frequency signal.

We use equation 4.42 and perform a first order Taylor expansion of $Re(\delta z^*)$ for $\omega_\Delta \ll \omega_c$.

$$Re(\delta z^*(\omega_i)) = Re(\delta z^*(\omega_c)) + \frac{\partial Re(\delta z^*)}{\partial \omega} \omega_\Delta \cos(\omega_L t) \tag{4.49}$$

Therefore, the low frequency current

$$I_{\omega_L}^{FM} = \frac{1}{2} \frac{\partial^2 I}{\partial V_{sd} \partial z} V_{sd} \frac{\partial Re(\delta z^*)}{\partial \omega} \omega_\Delta \cos(\omega_L t) \tag{4.50}$$

The above formula can be further simplified. If we ignore the nonlinearity between I and V_{sd},

$$\frac{\partial I}{\partial V_{sd}} = \frac{1}{R} = G \tag{4.51}$$

The conductance G is a function of the charge q on the graphene-gate capacitor. And q is a function of gate voltage V_g and distance between the graphene sheet and the back gate z.

Since V_g is fixed, z is the only variable.

$$G(V_g, z) = G(V_g, z_s) + \frac{\partial G}{\partial q}\frac{\partial q}{\partial z}\tilde{z} \tag{4.52}$$

Because

$$\frac{\partial G}{\partial q} = \frac{\partial G}{\partial V_g}\frac{\partial V_g}{\partial q} = \frac{\partial G}{\partial V_g}\frac{1}{C} \tag{4.53}$$

and

$$\frac{\partial q}{\partial z} = \frac{\partial q}{\partial C}\frac{\partial C}{\partial z} = V_g C' \tag{4.54}$$

so

$$G(V_g, z) = G(V_g, z_s) + \frac{\partial G}{\partial V_g}\frac{C'}{C}V_g\tilde{z} \tag{4.55}$$

Plug equation 4.51 and equation 4.55 into equation 4.50, we find the final expression for the low frequency current signal in FM technique.

$$I_{\omega_L}^{FM} = \frac{1}{2}\frac{\partial G}{\partial V_g}\frac{C'}{C}V_g V_{sd}\frac{\partial Re(\delta z^*)}{\partial \omega}\omega_\Delta \cos(\omega_L t) \tag{4.56}$$

Remarkably, unlike the $I_{\omega_L}^{AM}$ which has an undesirable background term, $I_{\omega_L}^{FM}$ gives a pure electromechanical signal. Also note that the current magnitude is proportional to the transconductance $\frac{\partial G}{\partial V_g}$, which can be greatly improved at low temperature and after current annealing, as mentioned in section 2.7. So it's a good practice to cool down the sample to liquid helium temperature and do a current anneal before taking real measurements.

4.6 Experimental Setup

The circuit and experimental setup is first designed by Dr. Hsin-Ying Chiu [8] and later modified by Dr. Tengfei Miao [32]. We follow their thesis to introduce the design.

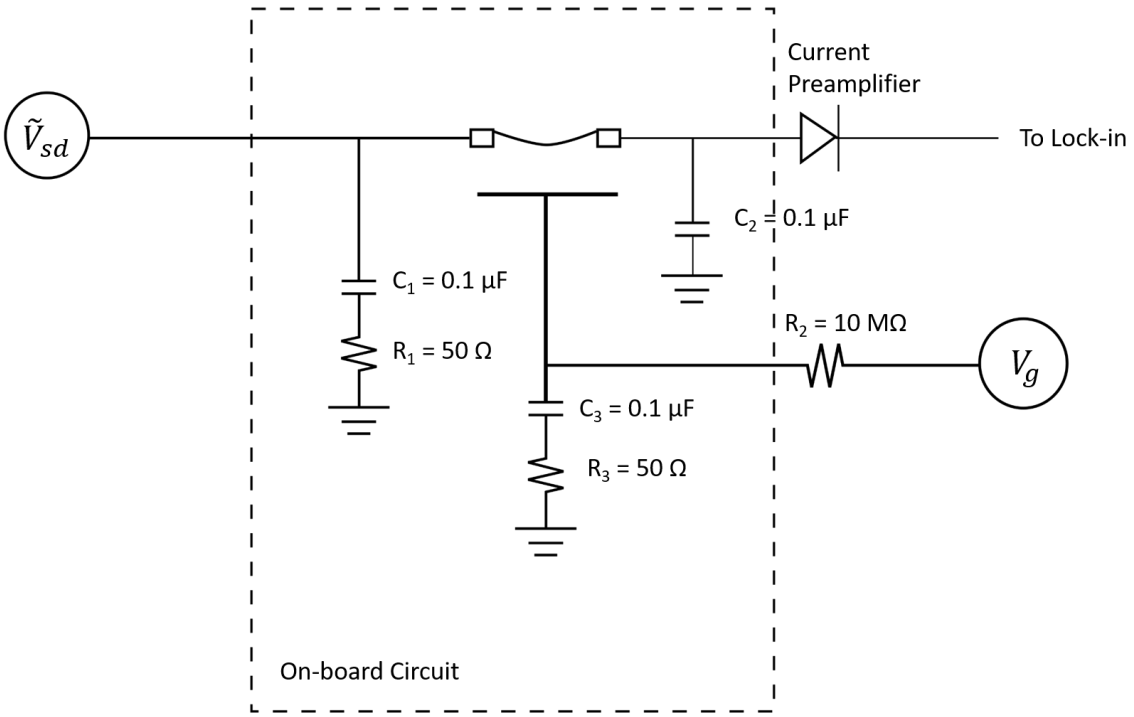

Figure 4.2: A schematic diagram of the measurement circuit.

4.6.1 Circuit Design

The circuit design is shown in Figure 4.2. As mentioned before, the biggest challenge in the design is to match the impedance. The impedance in the transmission line is typically 50 Ω, but the resistance in graphene nanoribbon is on the order of KΩ. To match the impedance in order to maximize the power transmitted to the device, we connect a 50 Ω resistor R_1 in parallel to the device. Therefore, the impedance V_{sd} sees is 50 Ω. To route V_{sd}^{DC} to go through the device rather than go through resistor R_1 to the ground, we add a capacitor C_1 to stop the DC signal.

After the signal is mixed by the graphene nanoribbon, we use a capacitor C_2 to short the high frequency signal. In the experiment, the typical resonance frequency is 100 MHz and the modulation frequency is 1 KHz. The impedance of the capacitor C_2 respect to the two signals are

$$X_{hf} = \frac{1}{i\omega_{hf}C_2} = \frac{1}{i \times 100Mhz \times 0.1\mu F} \sim 0.1\Omega$$

and

$$X_{lf} = \frac{1}{i\omega_{lf}C_2} = \frac{1}{i \times 1Khz \times 0.1\mu F} \sim 10^4\Omega$$

Therefore, the high frequency signal is effectively routed to the ground, and the low frequency signal is routed to the current preamplifier.

The gate voltage V_g is usually on the order of 10 V, which can generate a large current if the circuit is shorted. We use a large resistor R_2 for protection.

The configuration of C_3 and R_3 is symmetric to C_1 and R_1. It's not necessary in this thesis. However, it's useful if we want to fix V_{sd} and put a AC signal on V_g.

4.6.2 Equipment Setup

Because graphene resonance cannot be observed in the atmosphere because of air friction, and as mentioned in section 4.5, the signal is more prominent at low temperature, the system needs to be operated at high vacuum and low temperature. After careful design, we home made a cryostat as our measurement system. The whole system is about 140 cm in length. The sample is mounted on the sample holder shown in Figure 4.3. The whole

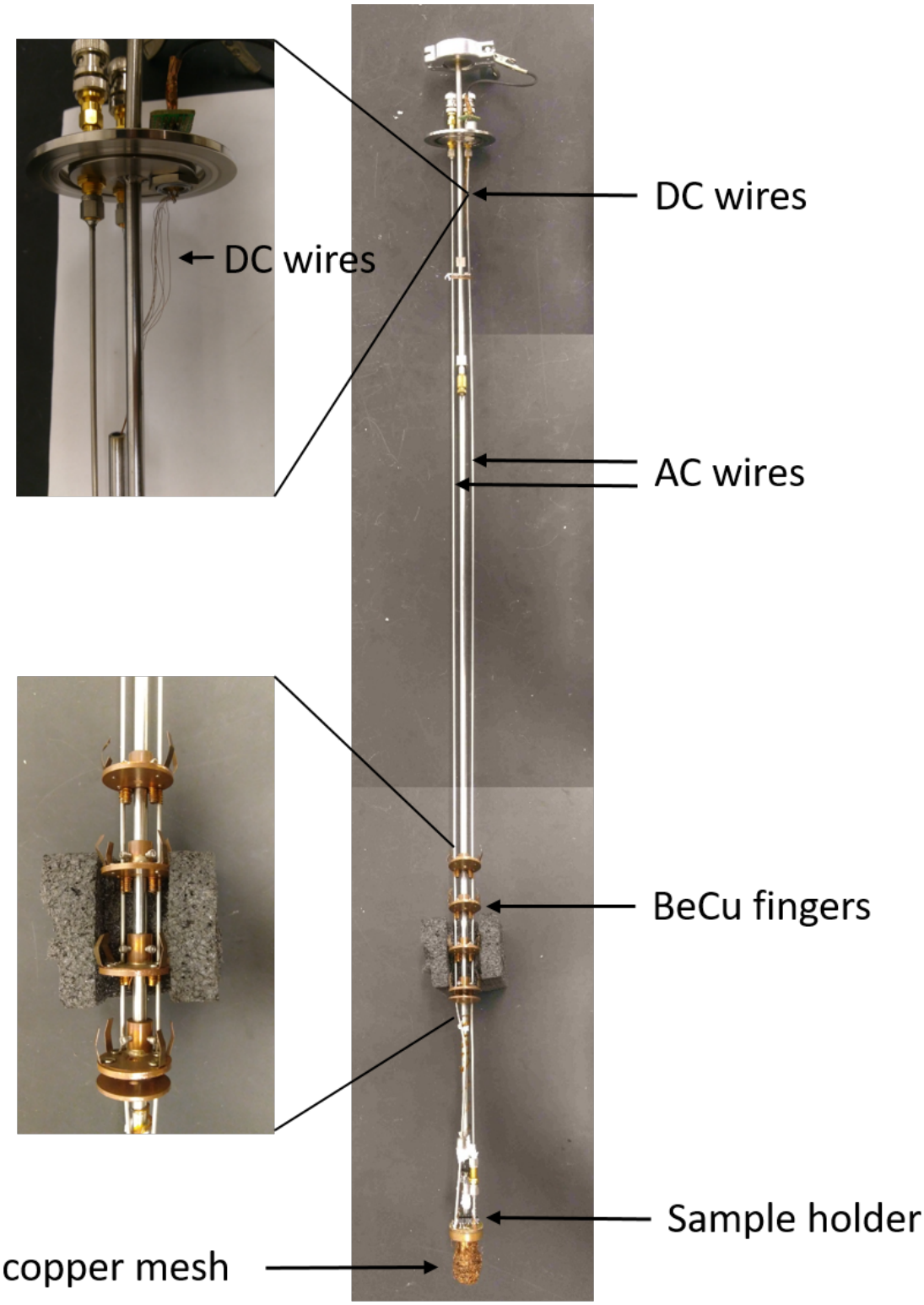

Figure 4.3: A picture of the internal stick of the home made cryostat.

stick below the top cap is enclosed in a one-piece sample chamber which can be pumped to high vacuum.

The system contains six DC wires. Two of the DC wires are connected to a thermal diode attached to the sample holder. The other four are connected to the sample holder. The system also include two AC wires, which are also connected to the sample holder. The DC and AC wires are soldered the sample holder, so we need to keep those pin locations in mind when bonding the device to the chip carrier. We connect two of the DC wires to a thermal diode to monitor the device temperature in situ. We connect the other two DC wires to the device.

To cool down the system, we first pump the sample chamber to high vacuum, then inject exchange gas to the chamber and slowly insert the system into liquid Helium. We use the thermal diode to monitor the temperature. When the temperature is stable at liquid Helium temperature, we pump out the exchange gas to allow a friction free environment for mechanical vibration. During the measurement, both mechanical motion and Joule effect generate heat. We further added the BeCu fingers and copper mesh to conduct the heat out of the system. The fingers are flexible that can easily slide in and out in the sample chamber and simultaneously contact the chamber firmly. The mesh contacts the bottom of the chamber and can provide cushion when loading the stick in the chamber. They are both below the liquid Helium level to allow optimal heat conduction.

Chapter 5

Nonlinear Dynamics at Various Temperatures

5.1 Introduction

We viewed the linear oscillator in section 1.4. The restoring force is linear elastic and the oscillator obeys Hooke's law. And the friction is a linear function of the velocity.

$$m\frac{d^2z}{dt^2} + m\omega_0^2 z + \Gamma\frac{dz}{dt} = F_0 cos(\omega t) \tag{5.1}$$

The above equation is a good approximation of the mechanical motion when the oscillation amplitude z is small. However, when we increase the drive, the system can be driven into the nonlinear regime and we need to consider the Duffing term αz^3 and nonlinear damping term $\eta z^2 \frac{dz}{dt}$.

$$m\frac{d^2z}{dt^2} + m\omega_0^2 z + \Gamma\frac{dz}{dt} + \alpha z^3 + \eta z^2\frac{dz}{dt} = F_0 cos(\omega t) \tag{5.2}$$

In this chapter, we discuss the nonlinear mechanical motion in graphene nanoribbons, and how the nonlinearity changes with temperature.

5.2 Nonlinear Dynamics

There are two additional terms shown in 5.2, the Duffing term and the nonlinear damping term. There are two main sources of nonlinearities: the external potential and tension change caused by geometry [29].

5.2.1 Nonlinearity Due to External Potential

We consider the potential energy of the resonator [29] in the following form

$$U(z) = \frac{1}{2}Kz^2 - \frac{C}{d+z} \tag{5.3}$$

where K is the effective elastic spring constant, C is a constant, d is the equilibrium separation between the resonator and the back gate when $V_g = 0$, z is the deviation from the equilibrium position. When we apply a voltage to the back gate, the graphene nanoribbon is pulled towards the gate and results in a new equilibrium position z_0. We consider an oscillation with amplitude δz. $\delta z = z - z_0$.

$$\begin{aligned} U(\delta z) &\simeq U(z_0) + \frac{1}{2}(K - \frac{2C}{(d+z_0)^3})\delta^2 z + \frac{C}{(d+z_0)^4}\delta^3 z + \frac{C}{(d+z_0)^5}\delta^4 z \\ &= U(z_0) + \frac{1}{2}k\delta^2 z + \frac{1}{3}\beta\delta^3 z + \frac{1}{4}\alpha\delta^4 z \end{aligned} \tag{5.4}$$

It yields a nonlinear equation of motion by solving $\frac{dU}{d\delta z} = 0$

$$m\frac{d^2\delta z}{dt^2} + k\delta z + \beta\delta^2 z + \alpha\delta^3 z = 0 \tag{5.5}$$

5.2.2 Nonlinearity Due to Geometry

The graphene nanoribbon is clamped at both ends, so its length changes when it oscillates. (We don't consider the case where the nanoribbon is not securely clamped, which can lead to parametric oscillation.) This effect can be neglected if oscillation amplitude is smaller than the nanoribbon width. However, as graphene is atomically thin, when the drive is strong, the oscillation amplitude can easily exceed its width. For a transverse displacement $X(z,t)$ from equilibrium, the Euler-Bernoulli equation is

$$\rho S\frac{\partial^2 X}{\partial t^2} = -EI\frac{\partial^4 X}{\partial z^4} + T\frac{\partial^2 X}{\partial z^2} \tag{5.6}$$

where ρ is the mass density, S the cross-section area, E the Young's modulus, I the moment of inertia, T the tension in the ribbon, z the coordinate along the ribbon. The equilibrium length of the ribbon is L, and the elongation due to oscillation is ΔL.

$$\begin{aligned} L + \Delta L &= \int_0^L dz\sqrt{1 + (\frac{\partial X}{\partial z})^2} \\ &\simeq L + \frac{1}{2}\int_0^L dz(\frac{\partial X}{\partial z})^2 \end{aligned} \tag{5.7}$$

Clearly, ΔL introduces nonlinear term in equation 5.6

5.2.3 Nonlinear Behavior

Adding the Duffing term and nonlinear damping term to the linear oscillation equation yields the nonlinear equation of motion.

$$m\frac{d^2z}{dt^2} + m\omega_0^2 z + \Gamma\frac{dz}{dt} + \alpha z^3 + \eta z^2\frac{dz}{dt} = F_0 cos(\omega t) \tag{5.8}$$

Solving this equation [29] gives the relation between the maximum response frequency ω_{max} and the oscillation magnitude z_0.

$$\omega_{max} = \omega_0 + \frac{3}{8}\frac{\alpha}{m\omega_0}z_0^2 \tag{5.9}$$

where ω_0 is the linear response peak frequency.

When the oscillation magnitude z_0 increases, the peak frequency shifts. If $\alpha > 0$, the frequency shifts to a larger value. This corresponds to the oscillation on a more tensioned string, and is called stiffening. On the other hand, if $\alpha < 0$, the frequency shifts to a smaller value. This corresponds to the oscillation on a less tensioned string, and is called softening. The two cases are both very common in experiments, and sometimes can happen on the same device with different drive V_{sd}, as shown in Figure 5.1.

We can also plot the oscillation magnitude and phase versus frequency as in Figure 5.2. The plot shows an example of Duffing oscillator response with positive α, therefore the peak shifts to the right. Line traces are plotted with different source-drain voltage. In the plot, we use a set of dimensionless parameters. The conversion between the regular parameters and dimensionless parameters can be found in the original paper [29].

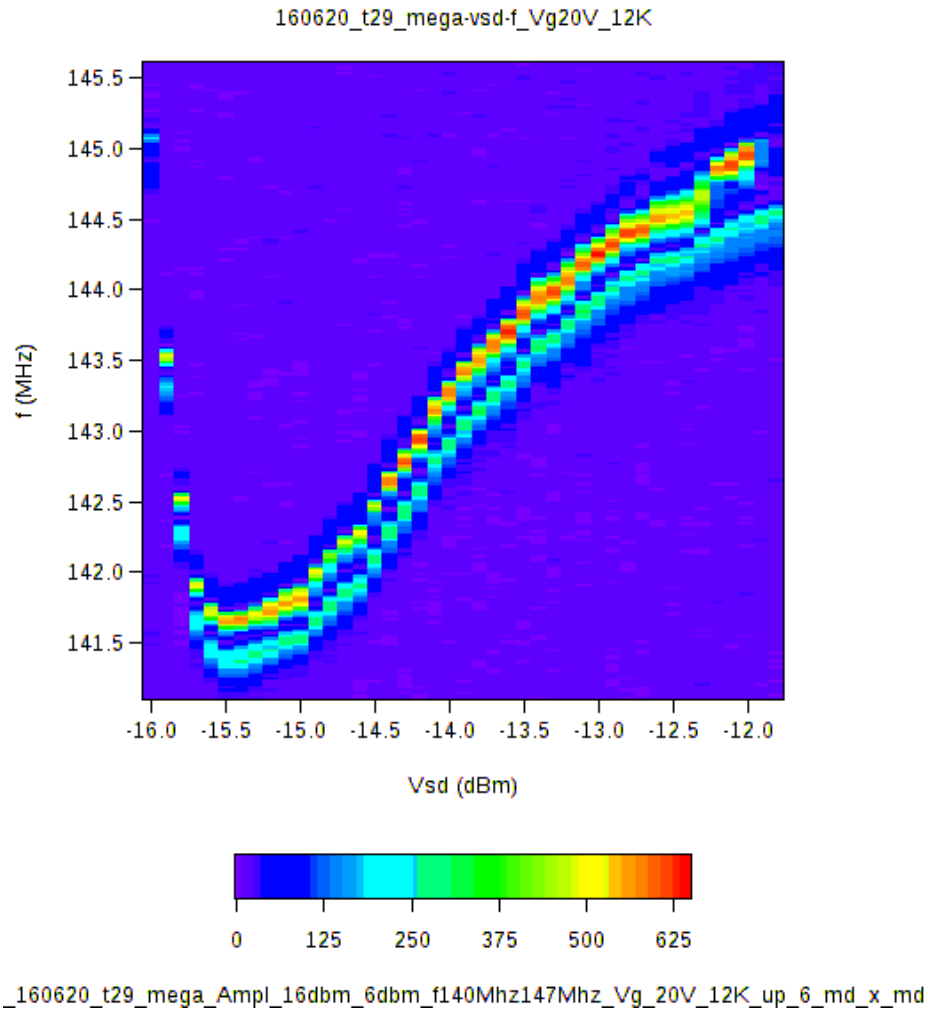

Figure 5.1: Duffing coefficient sign changes at different source-drain voltage. We see a α sign change from negative to positive when increasing the source-drain voltage continuously. As a result, the peak frequency ω_{max} first decreases, then increases, which is consistent with equation 5.9.

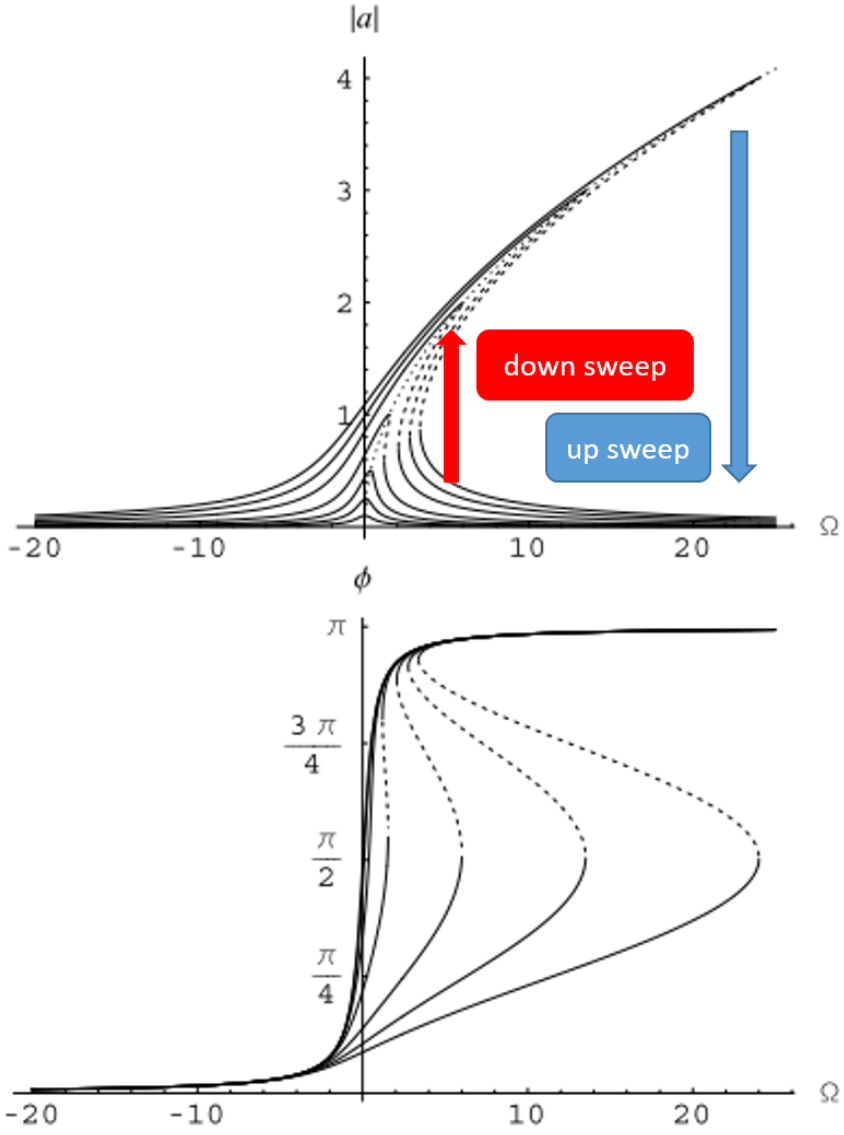

Figure 5.2: Magnitudes $|a|$ (top) and phases ϕ (bottom) of the response of a Duffing resonator as a function of the frequency Ω at different V_{sd}, without nonlinear damping ($\eta = 0$). Solid curves indicate stable solutions of the response function, while dashed curves indicate unstable solutions. (a) The blue arrow indicates the observation in a frequency up sweep. The oscillation magnitude follows the upper branch of the peak, increases up to a critical point and abruptly drops. The red arrow indicates the observation in a frequency down sweep. The oscillation magnitude follows the lower branch of the peak, increases up to a critical point and abruptly jumps to the upper branch, then follow the upper branch all the way to the left. The plots are adopted from paper [29].

Solving the nonlinear equation at large drive gives a saddle-node bifurcation in the solution. When the drive frequency is much smaller than the resonance frequency, we see only one solution. After the drive frequency increases up to a critical point, where we see two solutions, we see three solution. Among the three solutions, two are stable while the middle one is unstable. One of the stable solutions will be observed when we adopt a frequency sweeping direction. We see the upper branch solution and an abrupt oscillation magnitude drop when we sweep the frequency up. We see the lower branch solution and an abrupt oscillation magnitude increase when we sweep the frequency down.

We observe a frequency shift with positive α on most devices. We plot the mixing current as a function of frequency at different source-drain voltage in Figure 5.3.

5.3 Nonlinear Parameters

Revisiting the nonlinear equation of motion

$$m\frac{d^2z}{dt^2} + m\omega_0^2 z + \Gamma\frac{dz}{dt} + \alpha z^3 + \eta z^2\frac{dz}{dt}, = F_0 cos(\omega t) \tag{5.10}$$

the nonlinearity is described by two parameters, α and η. By solving the above equation, we find the expression for them in terms of the known parameters [33]. We first find the resonance amplitude $|\delta z|$.

$$|\delta z| = \frac{4d\delta I\delta f}{\frac{\partial G}{\partial V_g}V_{sd}V_g f_\Delta} \tag{5.11}$$

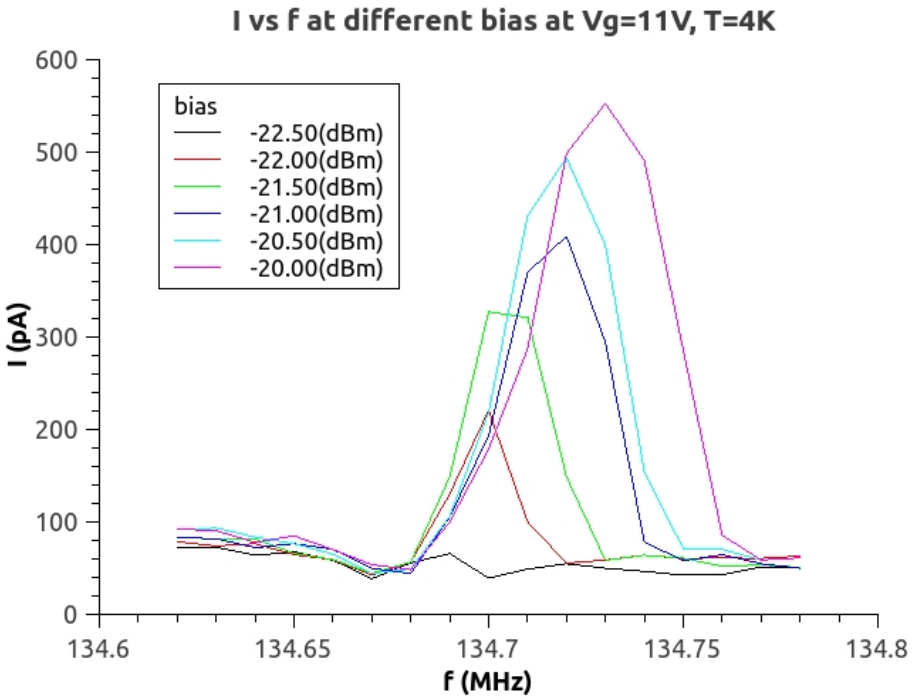

Figure 5.3: FM mixing current magnitude verses frequency at different source-drain voltage. We see a symmetric line trace at small V_{sd}. When drive increases, we see a transition from the linear regime to the nonlinear regime, and the line trace becomes more asymmetric. Measurement is taken at $V_g = 11$ V and temperature = 4 K.

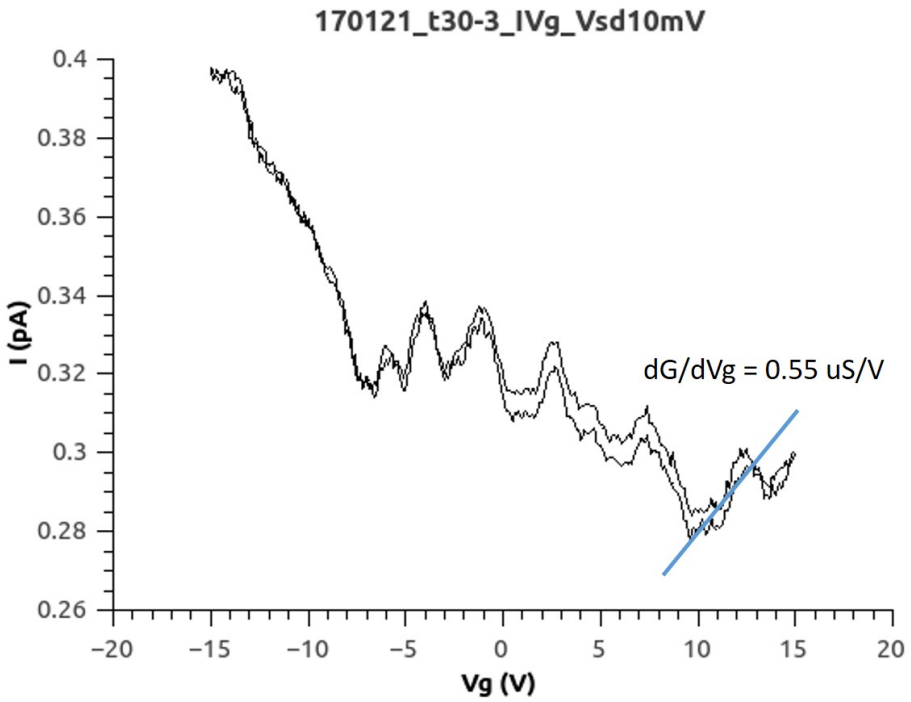

Figure 5.4: The transconductance at $V_g = 11$ V. It can be found by taking the derivative of the I-V_g curve then divided by V_{sd}. The source-drain voltage $V_{sd} = 10$ mV. Measurement is performed at 4.6 K.

where d the equilibrium separation between the back gate and the graphene nanoribbon (300 nm in our experiment, which is the thickness of SiO_2 layer), δI the mixing current, δf the width of the resonance peak, V_{sd} the source-drain voltage, V_g the gate voltage, f_Δ is frequency modulation amplitude (100 KHz in our experiment).

We use a fixed gate voltage V_g for simplicity and consistency of the dataset. We can find the transconductance $\frac{\partial G}{\partial V_g}$ at the V_g value we choose. In Figure 5.4 we find the transconductance at $V_g = 11$V.

Once we find the oscillation amplitude $|\delta z|$, we can use it to find the Duffing parameter α.

$$f_{res} = f_0 + \frac{3\alpha|\delta z|^2}{32\pi^2 f_0 m} \tag{5.12}$$

where f_{res} the resonance peak frequency, f_0 the linear response resonance frequency, m the mass of the graphene sheet. We etch the graphene to be nanoribbon with length 2 μm and width 0.2 μm. The mass density of graphene is $\rho_s = 7.6 \times 10^{-7}$ kg/m^2 [7].

We linear fit f_{res} vs. $|\delta z|^2$ to first find y-intercept f_0, then plug the value into the fitted slope to find α.

$$\frac{\alpha}{\eta} = 4\pi \frac{d\Delta f}{d\delta f} f_0 \tag{5.13}$$

Once α is obtained, we can plug it in equation 5.13 to find η, where $\Delta f = f_{res} - f_0$ is the frequency shift and δf is the width of the resonance frequency.

5.4 Nonlinear Mechanics at Various Temperatures

The temperature plays an important role in NEMS. Low temperatures not only usually give a larger transconductance $\frac{dG}{dV_g}$, resulting in a more prominent resonance signal, but also brings in thermal expansion effects and introduces less electron-phonon scattering. We expect the nonlinear behaviors are different at different temperatures.

Due to the increased $\frac{dG}{dV_g}$ and increased quality factor, the resonance signal is much stronger at lower temperatures. As shown in Figure 5.5, the resonance amplitude is much larger at a lower temperature, indicating a much stronger resonance. By linear fitting the data, we can use equation 5.12 to find the Duffing coefficient α. α equals 2.1×10^{11} N/m^3 at

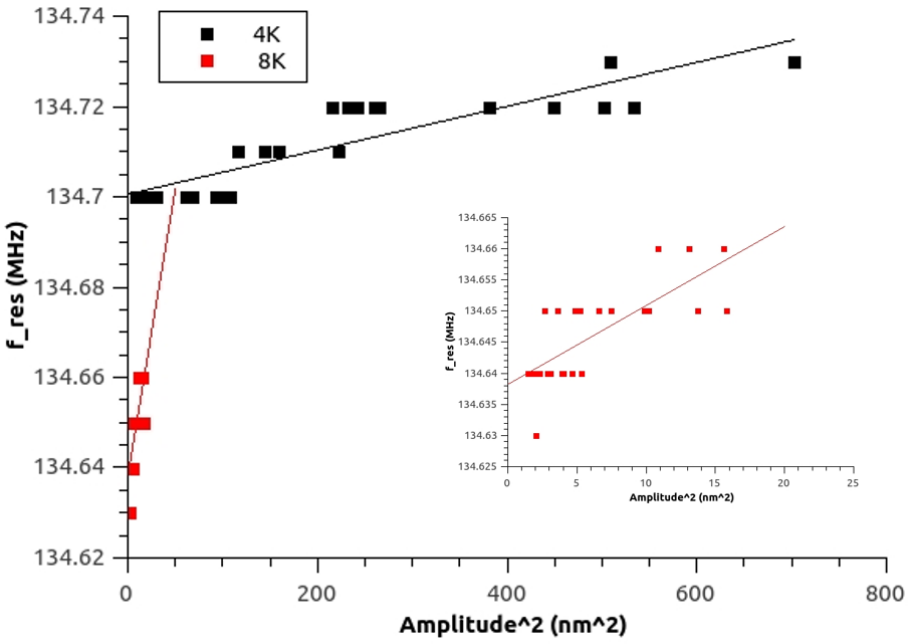

Figure 5.5: The figure shows the resonance frequency f_{res} is a linear function of squared resonance amplitude $|\delta z|^2$, and the inset is the zoom-in view of the data at 8K. Both data are measured with V_{sd} in range [-22 dBm (17.8 mV), -20 dBm (22.3 mV)]. At lower temperature, the resonance amplitude is much larger, indicating a much stronger resonance. We can use equation 5.12 to find the Duffing coefficient α by linear fit the data. $\alpha(4K) = 2.1 \times 10^{11}$ N/m^3, $\alpha(8K) = 5.5 \times 10^{12}$ N/m^3.

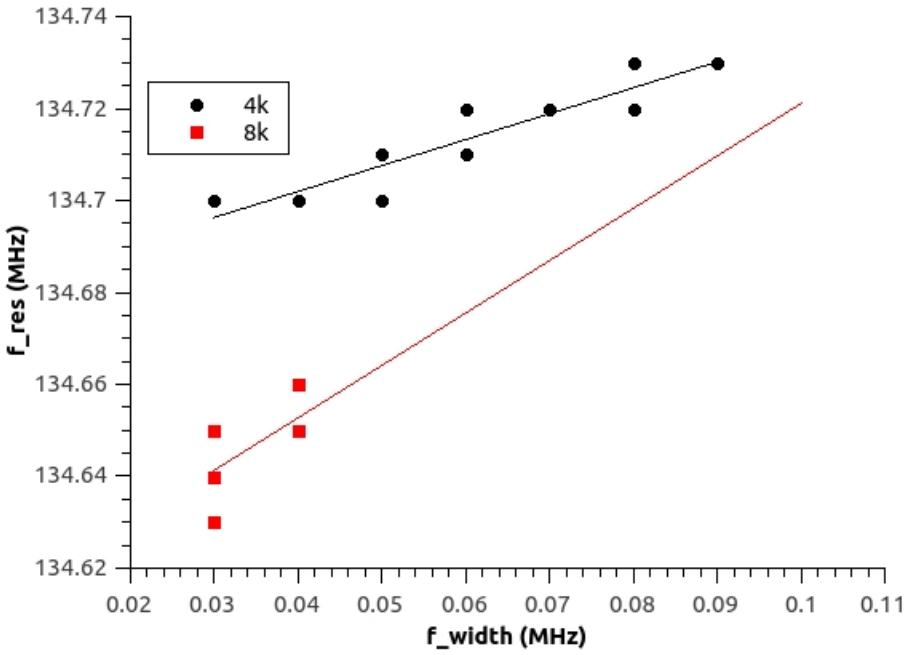

Figure 5.6: The figure shows the resonance frequency f_{res} is a linear function of the resonance peak width. Both data are measured with V_{sd} in range [-22 dBm (17.8 mV), -20 dBm (22.3 mV)]. At lower temperature, the quality factor Q (defined as $\frac{2f_{res}}{f_{width}}$) is higher. We can find the nonlinear damping coefficient η by linear fit the data. η (4K) = 288 Ns/m^3, η (8K) = 4421 Ns/m^3.

4K, and 5.5×10^{12} N/m^3 at 8K. The value increases by 20 times at the higher temperature.

We can also plot the resonance frequency as a function of the resonance peak width, as shown in Figure 5.6. Linear fit the data gives the $\frac{d\Delta f}{d\partial f}$ term in equation 5.13. Together with the Duffing coefficient α we find in Figure 5.5, we can find the nonlinear damping coefficient η. With η equals 288 Ns/m^3 at 4 K and 4421 Ns/m^3 at 8 K, we see a 20 times increase of η at the higher temperature, which aligns very wells with the change of α.

Chapter 6

Conclusions

6.1 Conclusion

In this thesis, we combined the electrical and mechanical properties of graphene and fabricated nano-scale mechanical resonators. We drove the source-drain voltage sufficiently large to saw the transition from the linear resonance regime to the nonlinear resonance regime. We applied frequency modulation technique and measured the Duffing coefficient and nonlinear damping coefficient at different temperatures. We also observed a sign change of the Duffing coefficient when applying different source-drain voltage.

In addition, we developed shadow mask, a super clean technique enables rapid and lithography-free device fabrication. We developed a stable recipe that has 70% throughout yield ratio. The alignment precision can be as accurate as 1 μm.

6.2 Future Work

People usually see positive α (Duffing coefficient) or negative α on different devices. We reported the sign change of α for the first time. The cause of the change is not yet clear. More devices and more careful measurements need to be done to confirm this behavior. Theoretical work also need to be developed for better understanding.

There are two sources contributing to the quality factor in mechanical resonators: energy dissipation and phase decoherence. The quality factor obtained in spectral response is sensitive to both dissipation and dephasing, while the quality factor obtained in ringdown measurement is sensitive to only dephasing. With increased driving power, both quality factors will be affected by the nonlinear effect [40]. It will be interesting to investigate these two quality factors' dependence on temperature in the nonlinear resonance regime.

Bibliography

[1] Walid Amamou, Patrick M Odenthal, Elizabeth J Bushong, Dante J OHara, Yunqiu Kelly Luo, Jeremiah van Baren, Igor Pinchuk, Yi Wu, Adam S Ahmed, Jyoti Katoch, et al. Large area epitaxial germanane for electronic devices. *2D Materials*, 2(3):035012, 2015.

[2] Wenzhong Bao, Gang Liu, Zeng Zhao, Hang Zhang, Dong Yan, Aparna Deshpande, Brian LeRoy, and Chun Ning Lau. Lithography-free fabrication of high quality substrate-supported and freestanding graphene devices. *Nano Research*, 3(2):98–102, 2010.

[3] I Bargatin, EB Myers, J Arlett, B Gudlewski, and ML Roukes. Sensitive detection of nanomechanical motion using piezoresistive signal downmixing. *Applied Physics Letters*, 86(13):133109, 2005.

[4] Arthur W Barnard, Vera Sazonova, Arend M van der Zande, and Paul L McEuen. Fluctuation broadening in carbon nanotube resonators. *Proceedings of the National Academy of Sciences*, 109(47):19093–19096, 2012.

[5] KI Bolotin, KJ Sikes, J Hone, HL Stormer, and Ph Kim. Temperature-dependent transport in suspended graphene. *Physical review letters*, 101(9):096802, 2008.

[6] Kirill I Bolotin, KJ Sikes, Zd Jiang, M Klima, G Fudenberg, J Hone, Ph Kim, and HL Stormer. Ultrahigh electron mobility in suspended graphene. *Solid State Communications*, 146(9):351–355, 2008.

[7] Jian-Hao Chen, Chaun Jang, Shudong Xiao, Masa Ishigami, and Michael S Fuhrer. Intrinsic and extrinsic performance limits of graphene devices on sio2. *Nature nanotechnology*, 3(4):206–209, 2008.

[8] Hsin-Ying Chiu. *Thermal properties and nanoelectromechanical system based on carbon nanotubes*. PhD thesis, California Institute of Technology, 2009.

[9] Hsin-Ying Chiu, Peter Hung, Henk W Ch Postma, and Marc Bockrath. Atomic-scale mass sensing using carbon nanotube resonators. *Nano letters*, 8(12):4342–4346, 2008.

[10] Andrew N Cleland and Michael L Roukes. Fabrication of high frequency nanometer scale mechanical resonators from bulk si crystals. *Applied Physics Letters*, 69(18):2653–2655, 1996.

[11] A Eichler, Joel Moser, J Chaste, M Zdrojek, I Wilson-Rae, and Adrian Bachtold. Nonlinear damping in mechanical resonators made from carbon nanotubes and graphene. *Nature nanotechnology*, 6(6):339–342, 2011.

[12] Alexander Eichler, Julien Chaste, Joel Moser, and Adrian Bachtold. Parametric amplification and self-oscillation in a nanotube mechanical resonator. *Nano letters*, 11(7):2699–2703, 2011.

[13] Artur Erbe and Robert H Blick. Silicon-on-insulator based nanoresonators for mechanical mixing at radio frequencies. *IEEE transactions on ultrasonics, ferroelectrics, and frequency control*, 49(8):1114–1117, 2002.

[14] IW Frank, David M Tanenbaum, AM Van der Zande, and Paul L McEuen. Mechanical properties of suspended graphene sheets. *Journal of Vacuum Science & Technology B: Microelectronics and Nanometer Structures Processing, Measurement, and Phenomena*, 25(6):2558–2561, 2007.

[15] Ruiping Gao, Zhong L Wang, Zhigang Bai, Walter A de Heer, Liming Dai, and Mei Gao. Nanomechanics of individual carbon nanotubes from pyrolytically grown arrays. *Physical Review Letters*, 85(3):622, 2000.

[16] Andre K Geim and Konstantin S Novoselov. The rise of graphene. *Nature materials*, 6(3):183–191, 2007.

[17] Vincent Gouttenoire, Thomas Barois, Sorin Perisanu, Jean-Louis Leclercq, Stephen T Purcell, Pascal Vincent, and Anthony Ayari. Digital and fm demodulation of a doubly clamped single-walled carbon-nanotube oscillator: Towards a nanotube cell phone. *Small*, 6(9):1060–1065, 2010.

[18] Ali Husain, J Hone, Henk W Ch Postma, XMH Huang, T Drake, Mladen Barbic, Axel Scherer, and ML Roukes. Nanowire-based very-high-frequency electromechanical resonator. *Applied Physics Letters*, 83(6):1240–1242, 2003.

[19] B Ilic, S Krylov, K Aubin, R Reichenbach, and HG Craighead. Optical excitation of nanoelectromechanical oscillators. *Applied Physics Letters*, 86(19):193114, 2005.

[20] Matthias Imboden, Oliver A Williams, and Pritiraj Mohanty. Observation of nonlinear dissipation in piezoresistive diamond nanomechanical resonators by heterodyne downmixing. *Nano letters*, 13(9):4014–4019, 2013.

[21] P Ivaldi, J Abergel, MH Matheny, LG Villanueva, RB Karabalin, ML Roukes, P Andreucci, S Hentz, and E Defay. 50 nm thick aln film-based piezoelectric cantilevers for gravimetric detection. *Journal of Micromechanics and Microengineering*, 21(8):085023, 2011.

[22] Hyun S Kim, Hua Qin, and Robert H Blick. Direct mechanical mixing in a nanoelectromechanical diode. *Applied Physics Letters*, 91(14):143101, 2007.

[23] MD LaHaye, J Suh, PM Echternach, Keith C Schwab, and Michael L Roukes. Nanomechanical measurements of a superconducting qubit. *Nature*, 459(7249):960–964, 2009.

[24] Lev Davidovich Landau, EM Lifshitz, and LP Pitaevskii. Statistical physics, part i, 1980.

[25] B Lassagne, D Garcia-Sanchez, A Aguasca, and A Bachtold. Ultrasensitive mass sensing with a nanotube electromechanical resonator. *Nano letters*, 8(11):3735–3738, 2008.

[26] Changgu Lee, Xiaoding Wei, Jeffrey W Kysar, and James Hone. Measurement of the elastic properties and intrinsic strength of monolayer graphene. *science*, 321(5887):385–388, 2008.

[27] Jingjing Li and S Evoy. Study of laser-induced self-oscillations in silicon nanomechanical resonators. *Journal of applied physics*, 98(8):084316, 2005.

[28] Xuesong Li, Carl W Magnuson, Archana Venugopal, Jinho An, Ji Won Suk, Boyang Han, Mark Borysiak, Weiwei Cai, Aruna Velamakanni, Yanwu Zhu, et al. Graphene films with large domain size by a two-step chemical vapor deposition process. *Nano letters*, 10(11):4328–4334, 2010.

[29] Ron Lifshitz and MC Cross. Nonlinear dynamics of nanomechanical and micromechanical resonators. *Review of nonlinear dynamics and complexity*, 1:1–52, 2008.

[30] Warren A Marrison. The evolution of the quartz crystal clock. *Bell Labs Technical Journal*, 27(3):510–588, 1948.

[31] JW McClure. Diamagnetism of graphite. *Physical Review*, 104(3):666, 1956.

[32] Tengfei Miao. Graphene nanoelectromechanical systems. 2015.

[33] Tengfei Miao, Sinchul Yeom, Peng Wang, Brian Standley, and Marc Bockrath. Graphene nanoelectromechanical systems as stochastic-frequency oscillators. *Nano letters*, 14(6):2982–2987, 2014.

[34] Joel Moser, Amelia Barreiro, and Adrian Bachtold. Current-induced cleaning of graphene. *Applied Physics Letters*, 91(16):163513, 2007.

[35] AH Castro Neto, F Guinea, Nuno MR Peres, Kostya S Novoselov, and Andre K Geim. The electronic properties of graphene. *Reviews of modern physics*, 81(1):109, 2009.

[36] Kostya S Novoselov, Andre K Geim, Sergei V Morozov, D Jiang, Y_ Zhang, Sergey V Dubonos, Irina V Grigorieva, and Alexandr A Firsov. Electric field effect in atomically thin carbon films. *science*, 306(5696):666–669, 2004.

[37] E Ollier, C Dupré, G Arndt, J Arcamone, C Vizioz, L Duraffourg, E Sage, A Koumela, S Hentz, G Cibrario, et al. Ultra-scaled high-frequency single-crystal si nems resonators and their front-end co-integration with cmos for high sensitivity applications. In *Micro Electro Mechanical Systems (MEMS), 2012 IEEE 25th International Conference on*, pages 1368–1371. IEEE, 2012.

[38] Aaron D OConnell, Max Hofheinz, Markus Ansmann, Radoslaw C Bialczak, Mike Lenander, Erik Lucero, Matthew Neeley, Daniel Sank, H Wang, M Weides, et al. Quantum ground state and single-phonon control of a mechanical resonator. *Nature*, 464(7289):697–703, 2010.

[39] Philippe Poncharal, ZL Wang, Daniel Ugarte, and Walt A De Heer. Electrostatic deflections and electromechanical resonances of carbon nanotubes. *science*, 283(5407):1513–1516, 1999.

[40] Ben H Schneider, Vibhor Singh, Warner J Venstra, Harold B Meerwaldt, and Gary A Steele. Observation of decoherence in a carbon nanotube mechanical resonator. *arXiv preprint arXiv:1503.06815*, 2015.

[41] K Schwab. Spring constant and damping constant tuning of nanomechanical resonators using a single-electron transistor. *Applied physics letters*, 80(7):1276–1278, 2002.

[42] JC Slonczewski and PR Weiss. Band structure of graphite. *Physical Review*, 109(2):272, 1958.

[43] Brian Standley, Wenzhong Bao, Hang Zhang, Jehoshua Bruck, Chun Ning Lau, and Marc Bockrath. Graphene-based atomic-scale switches. *Nano letters*, 8(10):3345–3349, 2008.

[44] JD Teufel, T Donner, MA Castellanos-Beltran, JW Harlow, and KW Lehnert. Nanomechanical motion measured with an imprecision below that at the standard quantum limit. *Nature nanotechnology*, 4(12):820–823, 2009.

[45] Georgia Tsoukleri, John Parthenios, Konstantinos Papagelis, Rashid Jalil, Andrea C Ferrari, Andre K Geim, Kostya S Novoselov, and Costas Galiotis. Subjecting a graphene monolayer to tension and compression. *small*, 5(21):2397–2402, 2009.

[46] Philip Richard Wallace. The band theory of graphite. *Physical Review*, 71(9):622, 1947.

[47] XC Zhang, EB Myers, JE Sader, and ML Roukes. Nanomechanical torsional resonators for frequency-shift infrared thermal sensing. *Nano letters*, 13(4):1528–1534, 2013.